PHOTOSPHERIC AND HELIOSPHERIC MAGNETIC FIELDS

CAROLUS J. SCHRIJVER and MARC L. DEROSA
Lockheed Martin Advanced Technology Center, Dept. L9–41, Bldg. 252, 3251 Hanover Street, Palo Alto CA 94304, U.S.A. (e-mail: schryver@ℓmsaℓ.com; derosa@ℓmsaℓ.com)

(Received 26 August 2002; accepted 24 September 2002)

Abstract. The magnetic field in the heliosphere evolves in response to the photospheric field at its base. This evolution, together with the rotation of the Sun, drives space weather through the continually changing conditions of the solar wind and the magnetic field embedded within it. We combine observations and simulations to investigate the sources of the heliospheric field from 1996 to 2001. Our algorithms assimilate SOHO/MDI magnetograms into a flux-dispersal model, showing the evolving field on the full sphere with an unprecedented duration of 5.5 yr and temporal resolution of 6 hr. We demonstrate that acoustic far-side imaging can be successfully used to estimate the location and magnitude of large active regions well before they become visible on the solar disk. The results from our assimilation model, complemented with a potential-field source-surface model for the coronal and inner-heliospheric magnetic fields, match *Yohkoh*/SXT and KPNO/He 10830 Å coronal hole boundaries quite well. Even subject to the simplification of a uniform, steady solar wind from the source surface outward, our model matches the polarity of the interplanetary magnetic field (IMF) at Earth $\sim$ 83% of the time during the period 1997–2001 (independent of whether far-side acoustic data are incorporated into the simulation). We find that around cycle maximum, the IMF originates typically in a dozen disjoint regions. Whereas active regions are often ignored as a source for the IMF, the fraction of the IMF that connects to magnetic plage with absolute flux densities exceeding 50 Mx cm^{-2} increases from $\lesssim$ 10% at cycle minimum up to 30–50% at cycle maximum, with even direct connections between sunspots and the heliosphere. For the overall heliospheric field, these fractions are $\lesssim$ 1% to 20–30%, respectively. Two case studies based on high-resolution TRACE observations support the direct connection of the IMF to magnetic plage, and even to sunspots. Parallel to the data assimilation, we run a pure simulation in which active regions are injected based on random selection from parent distribution functions derived from solar data. The global properties inferred for the photospheric and heliospheric fields for these two models are in remarkable agreement, confirming earlier studies that no subtle flux-emergence patterns or field-dispersal properties are required of the solar dynamo beyond those that are included in the model in order to understand the large-scale solar and heliospheric fields.

1. Introduction

The evolution of the magnetic field in the heliosphere, in combination with the rotation of the Sun, drives space weather as geospace is subjected to continual changes in the conditions of the solar wind and the magnetic field embedded within it. The heliospheric field is rooted in a small but significant fraction of the flux that penetrates the surface of the Sun: the typical absolute heliospheric flux is $\sim 4 \times 10^{22}$ Mx (varying by no more than a factor of about two over the years, e.g., Lockwood, 2002), compared to a total photospheric flux in the intrinsically strong

Solar Physics **212:** 165–200, 2003.

magnetic field that ranges from $\sim 20 \times 10^{22}$ Mx to $\sim 80 \times 10^{22}$ Mx from cycle minimum to maximum (e.g., Harvey, 1993). The heliospheric flux thus amounts to some 20% of the surface flux at cycle minimum and $\sim 5\%$ at cycle maximum; this anticorrelation reflects the change in the dominant field component from the large-scale polar-cap dipole to the smaller-scale field that is associated with the set of active regions and their decay products that dominate the field at cycle maximum. At an intrinsic field strength of 1–2 kG, the photospheric area from which that heliospheric field arises covers a mere $\sim 0.04\%$ of the solar surface. Understanding of the heliospheric field in general, and specifically of its geospace consequences, requires knowledge of the evolution of its sources, which in turn requires us to know where these sources are on the solar surface, how their large-scale patterns come about, and how important distinct types of sources are at different phases of the cycle.

The dominant source of heliospheric flux is the ensemble of large unipolar areas on the Sun from which field lines cannot close to nearby areas of opposite polarity. Field lines that reach high enough are then forced open by the solar wind, and continue outward into the heliosphere. The footprint of the open flux originating from such unipolar photospheric regions corresponds to the coronal holes that cover the solar polar regions during the least active phases, and to one or more lower-latitude coronal holes formed over the dispersing flux of decayed large active regions. It is from these regions that the fast solar wind originates (compare reviews by, e.g., Gosling, 1996, and Axford and McKenzie, 1990).

The complementary slow wind streams, and the field they carry, originate from multiple low- and mid-latitude unipolar areas whose envelope is often referred to collectively, and non-specifically, as the streamer belt. A significant source of heliospheric field within this streamer belt is associated directly with active regions. That active regions contribute to the heliospheric flux has already been mentioned in some early studies (e.g., Levine *et al.*, 1977; Švestka *et al.*, 1977; Levine, 1982), but how much they contributed was never explicitly quantified. In this study we elucidate how the heliospheric field connects to its photospheric source regions in unipolar and active regions, study the global properties of field geometry and evolution over the years, and discuss a few examples in some detail.

Our understanding of the sources and average structure of the magnetic field in the high corona and inner heliosphere was greatly advanced some four decades ago as a result of three ground-breaking papers. First, Parker (1958) discussed the solar wind and identified the characteristic spiral pattern of the heliospheric field that connects the field observed at the Earth's orbit to regions close to the Sun. Then, Leighton (1964) argued that the evolution of the surface field was governed by dispersal in the large-scale flows of the differential rotation and supergranular random walk, and – as recognized only years later by Mosher (1977; see also DeVore, Sheeley, and Boris, 1984, and references therein) – by the meridional flow. Schatten, Wilcox, and Ness (1969) approximated the connection between the surface field and the heliospheric field with the so-called source-surface model,

in which a potential field is made to become radial at some distance R_{ss} from the solar center. In the years since then, it has been demonstrated repeatedly (e.g., Levine, 1982; Wang and Sheeley, 1992) that the positions of the coronal holes, and the polarity pattern of the background interplanetary magnetic field (IMF) could be recovered quite accurately with the source-surface model, for a value of $R_{ss} \sim 2.5 R_{\odot}$ (e.g., Hoeksema, 1984). Recent modeling demonstrated that coronal hole configurations found with 3D MHD models agree well with those inferred from the source-surface modeling (Neugebauer *et al.*, 1998), supporting the use of the latter as a convenient, simple, fast approximating algorithm.

These conceptual models have enabled the investigation of many solar and heliospheric phenomena over the past four decades (key studies include DeVore *et al.*, 1985; Sheeley, Nash, and Wang, 1987; Wang and Sheeley, 1994; Wang, Sheeley, and Lean, 2000). With rapid advances in observational resources (SOHO, *Yohkoh*, TRACE, ACE, *Ulysses*, . . .), computer capacity and speed, and remote data access, a new opportunity for advanced study is emerging: high-resolution models can be made of the global solar field, extrapolated into the heliosphere, and compared to various observational constraints, and displayed to yield a quick overview of many related aspects of solar-heliospheric science. This study explores the quantitative potential of such an approach by combining space- and ground-based observations with numerical simulations for the period from July 1996 until December 2001, i.e., from the most recent solar minimum to past the subsequent solar maximum.

Using SOHO/MDI full-disk magnetograms as input to a flux-transport model, we are able to approximate the evolution of the photospheric magnetic field on the unobservable hemisphere of the Sun, and thus obtain a continuously evolving model of the surface field over the whole solar surface. We have chosen a temporal resolution of 6 h, rather than the often employed resolution of approximately one month for most of the Sun (dictated by the Sun's mean rotation period), which may be combined with daily updates of the field on the visible side of the Sun. This allows an unprecedented evaluation of processes on the Sun and in the inner heliosphere.

After a description of the algorithms (Section 2), we first demonstrate that the high-resolution, full-sphere assimilation model provides a good match to the observable signatures of the corona–heliosphere coupling (Section 3). We then proceed with an analysis of the statistical and global properties of the heliospheric and interplanetary magnetic fields, and their photospheric sources. Prior to a discussion of the conclusions, we close with two case studies of these sources, observed at high resolution, to support our finding that active regions, and even sunspots, contribute significantly to the heliospheric field.

2. Model

Our algorithm comprises three basic components: (A) the *flux-dispersal model* that approximates the evolution of the photospheric magnetic field, (B) the *data-assimilation procedure* with which SOHO/MDI near-side magnetograms and helioseismic far-side data are incorporated, and (C) the *source-surface potential-field model* by which the inner-heliospheric field is approximated. This section provides a synopsis of these components, and describes the assumptions, approximations, and initial conditions. The Appendices (numbered as above for the model components) provide more detailed descriptions and references to related studies based on these algorithms.

The flux-dispersal model used here is an enhanced version of the classical model developed by Wang, Sheeley, DeVore and colleagues: flux concentrations are transported in a combination of differential rotation, meridional flow, and supergranular random-walk (diffusive) dispersal (flux is described here as 'atomic particles' moving about on a sphere with no restricting grid, rather than as a continuous medium interpolated onto a grid as in the classical model). The model is described in detail by Schrijver (2001), Schrijver and Title (2001), and Schrijver, DeRosa, and Title (2002), who compare it with solar observations over the past few decades, data for stars of very different levels of activity, and solar data and a proxy for the heliospheric field from the Maunder minimum onward, respectively. These studies confirm that the model provides an accurate approximation to solar and global heliospheric conditions.

One key difference with the classical model is that the code can be set to inject bipolar regions ranging from large active regions to small ephemeral regions onto the model solar photosphere, using observed, time-dependent distributions of latitude, flux, and orientation, including nesting properties of successive generations of bipoles. This mode is used to generate an alternative, completely artificial model (M) to compare to two models (A and A_f, see below) into which SOHO/MDI magnetograms are assimilated to approximate the real Sun.

The simulation model (M) and the assimilation models (A and A_f) start from the same initial field distribution characteristic of the latest cycle minimum, taken from the simulation by Schrijver, DeRosa, and Title (2002), computed for 1996.5, the starting date of our present experiments. This initial condition has a total flux of 35×10^{22} Mx, a total absolute flux poleward of 60° in latitude of 3.1×10^{22} Mx, and a mean flux density for the field above 80° of 8.8 Mx cm^{-2}. With that flux density, close to the value inferred by Wang, Nash, and Sheeley (1989) for the preceding cycle minimum in 1986, the polarity inversion for the north pole (determined by looking at flux within 10° of the pole) occurs somewhere in the first half of 2001 (crossing zero twice in that period, and fluctuating near zero at other times), and

for the south pole around 2001.2 (much more clearly defined). Low-pass filtered data from the Wilcox Solar Observatory[1] are compatible with that timing.

The pure simulation model M is computed from 1996.5 through 2002.0 using sunspot numbers[2] to determine the flux-emergence rate, as in Schrijver, DeRosa, and Title (2002). For assimilation model A, SOHO/MDI magnetograms are assimilated within 60° from disk center, subject to the assumption that the field is strictly vertical, and without corrections for underestimated spot fields. This assimilation procedure is a straightforward mapping: after re-binning to a resolution of 8 arc sec, each magnetogram pixel is assumed to correspond to a single concentration at the corresponding latitude and longitude; once flux rotates out of the assimilation area, the code rapidly bunches these concentrations into clusters comparable to those on the rest of the sphere. In addition to the assimilated magnetograms, small magnetic bipoles ($|\Phi| < 2 \times 10^{20}$ Mx) are injected outside the assimilation area for models A and A_f according to the same procedures as in model M; this maintains the quiet-Sun network which impacts the flux dispersal even though it adds little to the large-scale coronal field at any given instant (see Schrijver, 2001, for a description of that nonlinear coupling in the model). All models are run with a time step of 6 hr, or 21 600 s, to keep the model and the SOHO/MDI full-disk observations approximately in step.

Far-side acoustic information[3] (see Lindsey and Braun (2000), and Braun and Lindsey (2001), for descriptions of the method) is included in a special model A_f, starting on 3 September 2000 from which time onward a continuous far-side image sequence is available. The initial condition for model A_f at that time is the matching magnetic configuration computed for the assimilation model A based only on the near-side SOHO/MDI magnetograms. Bipoles are inserted on the far-side of the Sun depending on the pattern and magnitude of the measured travel-time differences of *p* modes reflecting around the antipode of disk center (see Appendix).

The coronal and inner-heliospheric fields are approximated with a potential-field extrapolation that assumes that the coronal field is potential everywhere between the photosphere (where only the radial component of the field is matched) and a spherical source surface (where the field is forced to become purely radial). Except for the detailed studies discussed in Section 7, we use a resolution equivalent to 64 elements in latitude and 128 elements in longitude, roughly equivalent to a grid-point spacing of 3° at the equator. The field is computed after removing any existing monopole component (because of incomplete assimilation of magnetic information – see Section 3.3). Note that there is, by definition, no monopole in the pure simulation model M. Each field extrapolation is based on magnetograms averaged over one-day intervals (4 time steps of the models).

[1]URL: http://quake.Stanford.EDU:80/~wso/gifs/north.gif and south.gif
[2]URL: http://www.sel.noaa.gov/SolarCycle/
[3]URL: http://soi.Stanford.EDU/data/farside/src/helio_FSI/

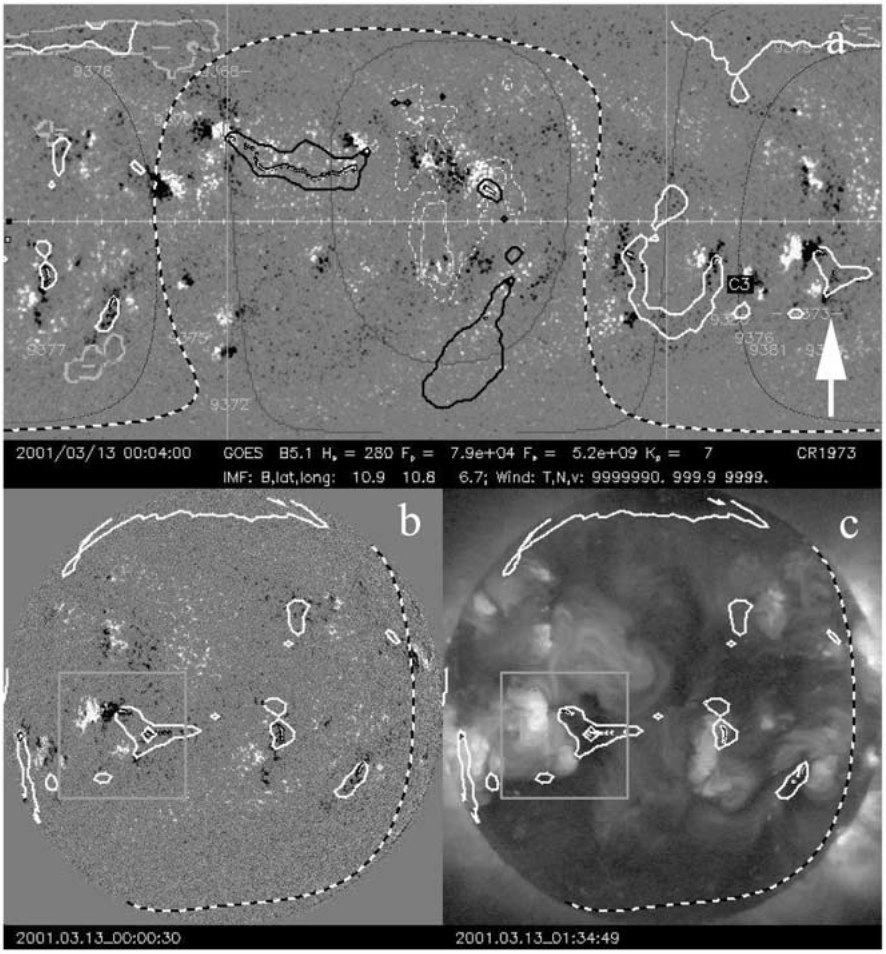

Figure 1 (a-c).

Figure 1. (a) Sample assimilation image (cf., Movies Ia and IIa on the CD-ROM): a $\sin(\theta) - \phi$ map of the photospheric magnetic field showing the 60° assimilation window (*large thin black oval*), front-back separators (*white vertical lines* 90° from 0° latitude at disk center), the far-side acoustic information (*thin dashed contours*), He 10830 Å coronal hole boundaries (*gray*), the projected current sheet (*black-white dashed*), the footprints of the open field (*black and white contours*) and of the equatorial IMF (*small dots*), and AR, flare, and filament-disappearance information. (b, c) SOHO/MDI magnetogram with contours of open field, and *Yohkoh*/SXT Al/Mg X-ray image with contours of open field (together shown in Movie III). See Appendix for further details. (d) MDI magnetogram detail (see gray square in panels (b) and (c)). (e) Blend of aligned TRACE 171 Å image and MDI magnetogram. (f) TRACE 171 Å image. (g) Detail of field extrapolation shown in Figure 13: open field lines are shown in *light gray*, closed field lines in *black*. The starting points of the field lines are determined by a random likelihood, proportional to the flux density in the magnetogram.

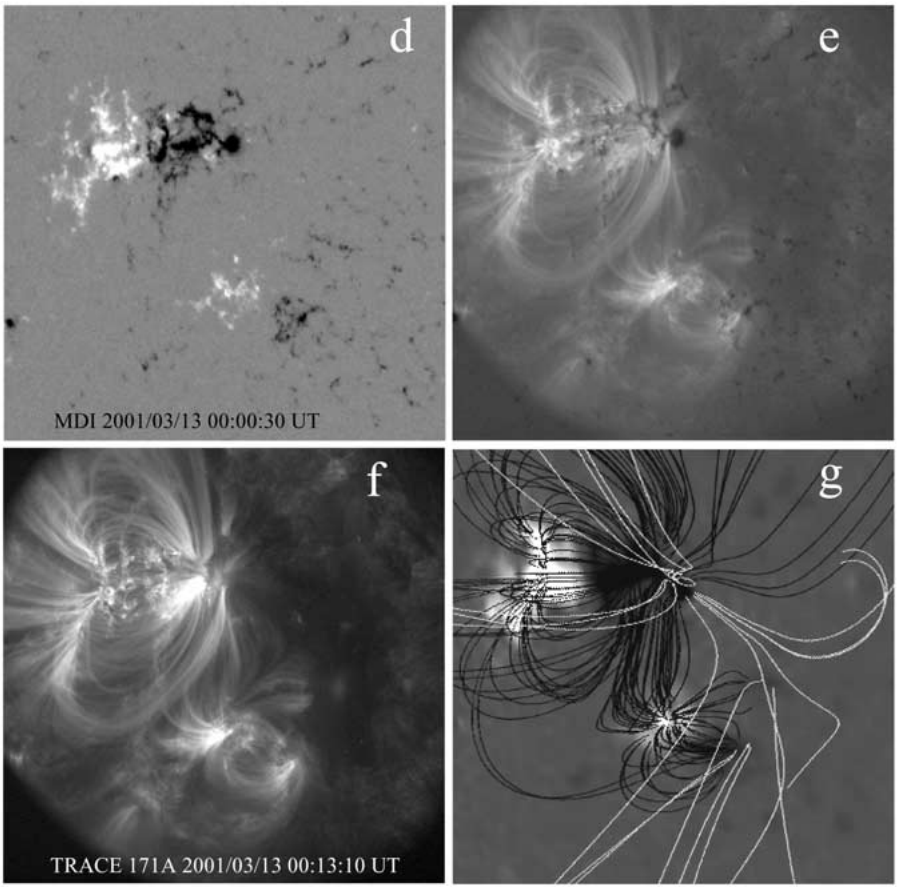

Figure 1 (d-g).

The connectivity of the heliosphere to the photosphere is subsequently computed for three sets of field lines: 360 equally spaced from the equatorial plane at the source surface, 2356 roughly equally spaced field lines distributed over the source surface, and another such set on the photosphere. This sampling allows us to trace the equatorial heliospheric field (as an approximation to the IMF, ignoring the 7° *b*-angle between solar equator and ecliptic) with 1° resolution. It enables us to map structures in the high-coronal field from compact strong sources (best found by inward tracing) and extended weak sources (best found by outward tracing).

For completeness and comparison, we add solar data on flares and filament disappearances, and He I 10830 Å coronal hole boundaries, and IMF and solar wind parameters (see Appendix), to the movies shown on the CD-ROM (compare Table I).

3. Simulations and Their Geometric Results

3.1. A DISCUSSION OF MODEL PARAMETERS AND MODEL RESULTS

Movie Ia shows the results of model A (magnetogram assimilation only) from the middle of 1996 through the end of 2001, as a sequence of maps in $\sin(\theta) - \phi$ format (for latitude θ and longitude ϕ). One of the most striking features of that sequence of full-sphere magnetograms is the role of nests of activity in which successive generations of magnetic bipoles emerge for periods lasting up to several months (e.g., Brouwer and Zwaan, 1990); Harvey and Zwaan (1993) estimate that at least one third of all active regions (and the flux they carry) form part of a nest, perhaps even more than half. As a result of this nesting, many active regions (many of which are part of active complexes formed by neighboring bipolar regions) appear to have strengthened or rejuvenated upon returning on the visible hemisphere after a two-week absence.

We found that these nested active regions place the most strict requirement on the rotation rate to be used for the assimilation model A: a good match of the patterns from rotation to rotation is found starting with the differential rotation profile of Komm, Howard and Harvey (1993) for small flux concentrations, but with the solid-body term increased by 0.2° day^{-1} to an equatorial (sidereal) rotation rate of 464.9 ± 1.5 nHz. That value matches the value of 464.4 nHz derived by Sheeley *et al.* (1992) based on a comparison of flux-dispersal models with Wilcox Solar Observatory data. It also equals the value for growing recurrent sunspots groups reported by Brajša *et al.* (2002). These authors find a value of 461.7 nHz for decaying groups; Brouwer and Zwaan (1990), in comparison, report an intermediate value of 463.7 ± 0.3 nHz, for all nests.

With this modified equatorial rotation rate, the movie shows good continuity not only for the active nests or long-lived active regions, but also for the unipolar areas formed by the decaying regions. Note that this also means that the effective flux dispersal coefficient (250 km^2 s^{-1} for concentrations with $\Phi = 1.6 \times 10^{19}$ Mx) used in the model is compatible with the observations. That dispersal coefficient is dependent on the flux in the concentrations matching an observed trend in the mobility of concentrations as a function of their flux; Schrijver *et al.* (1996) and Schrijver (2001) argue that this flux dependence likely explains why different diffusion coefficients are generally found for different methods of observation and modeling. The current results show that interpretation to be compatible with observations.

For the present purpose, the rotation profile and the dispersal coefficient do not lead to noticeable systematic discontinuities at the 'assimilation interface' on the eastern side of the central part of the MDI magnetograms, demonstrating that the model deviates from the real Sun by no more than about a degree per rotation. The study of any small residual difference is left to future investigations.

3.2. CORONAL HOLE PATTERNS AND THEIR EVOLUTION

Movie II shows the results of the field extrapolation into the corona overlayed on the images shown in Movie I. In discussing the results, we explicitly differentiate between various definitions of the term coronal hole. The term was first used by Waldmeier (1957) ('Koronalöcher') to describe the dark regions observed in the coronal green line over the solar poles during cycle minima. In the Skylab era, coronal holes were defined as either 'regions of strongly reduced coronal emission' (Huber *et al.*, 1974), or – equivalently – as 'extensive regions of extremely low density in the solar corona within 60° latitude from the equator' (Altschuler, Trotter, and Orrall, 1972, who interestingly exclude the prototypical coronal holes over the poles in that definition), as inferred from either deconvolved maps of the off-disk K-corona observed with coronagraphs or as observed directly on the disk in the extreme ultraviolet. The correspondence of regions of low emission (or electron density) with open magnetic fields that was found in many studies since then led Golub and Pasachoff (1997) to define coronal holes as 'open-field regions in the corona'. The meaning of the statement that 'essentially ALL interplanetary magnetic field lines are rooted in coronal holes' (Schwenn *et al.*, 1997) depends on which definition of coronal hole the authors had in mind. If extensive regions of reduced coronal emission that 'form from the remnants of active regions' (Wang and Sheeley, 1990b) are meant, then – as we argue in this study – the significant contribution of active regions to the heliospheric field is overlooked. If, on the other hand, 'coronal holes' are defined as open-field regions, the statement is no more than a definition.

A coronal hole is most unambiguously defined as a coherent dark patch in soft X-ray images of the solar corona; we refer to these as X-ray coronal holes, or XCH, and include in this definition the wide, irregular patches that are observable over most of the disk as well as the narrow dark channels that are observable only around the time of central-meridian passage. Comparison of ground-based (mostly chromospheric) He I 10830 Å synoptic maps and X-ray images demonstrated a general correspondence of XCHs to relatively bright areas in He I 10830 Å; we refer to the latter as 'chromospheric' coronal holes, or CCH. We note that narrow or small XCHs often do not show up as CCHs, likely because radiation from adjacent bright coronal regions does not allow the chromospheric signature to develop. The overall correspondence of XCHs to areas in which the high coronal magnetic field is (mostly) open into the heliosphere leads us to refer to footprint regions of open field found in our modeling as assimilation coronal holes, or ACH.

We find that most non-polar CCH structures correspond to ACH structures, best around central-meridian passage, as expected. ACH boundaries range from very stable structures, persisting in much of their geometry from day to day for up to months, and those that evolve seemingly erratically from step to step. Many composite structures are a mixture of the two, with parts relatively stable, and other segments of boundaries, or outlying islands, evolving rapidly. Our ACH boundaries

TABLE I.

List of QuickTime/Cinepak movies included on the CD-ROM[a].

– Movie Ia: Magnetic maps ($\sin(\theta) - \phi$) for the period 1996.5–2002.0 based on MDI magnetogram assimilation. The images are shown with $\sin(\theta)$ plotted versus Carrington longitude; the gray scale saturates at 30 Mx cm^{-2}. The oval shows the assimilation window (60° from apparent disk center for SOHO/MDI, identified by the small black-and-white square). The white vertical lines show longitudes 90° from disk center. Active region numbers are shown when available; dashes identify those observed with TRACE. The lower bar shows: the date and time of the assimilated magnetogram, the GOES soft X-ray level for that time, the sunspot coverage (in micro-hemispheres), the proton and electron fluences, and the planetary K_p index. The Carrington rotation number is shown on the right.
– Movie IIa: As movie Ia, also displaying solar, solar-wind, and heliospheric field data. He I 10830 Å coronal hole boundaries (light gray) for the front side of the Sun, flares (ordered by magnitude) and filament disappearances (and limb events) within 6 hr of the time. The lower line in the text bar includes the IMF field strength (nT), and the field latitude and longitude angles (in degrees) in Geocentric Solar Ecliptic coordinates, followed by the wind proton temperature (K), density (per cubic centimeter) and speed (km s^{-1}). The dashed line is a projection of the current sheet onto the photosphere; solid lines are contours around areas where field lines connect the photosphere to the source surface, shown in black and white for opposite polarities. Small diamonds are used to identify footpoints of field lines starting from the equatorial plane on the source surface; a large diamond identifies the footpoint of the field line connected to the subsolar point. The far-side data (not used in this assimilation) is also shown for comparison by thin white contours. The black oval around the antipode of disk center shows the edge of the field of view for the far-side images. Thin black curves around the white vertical lines separate front from back as seen by MDI at the time of the far-side image that was assimilated.
– Movie IIb: As Movie IIa, based on MDI magnetogram assimilation combined with far-side acoustic data.
– Movie III: MDI magnetograms and SXT Al/Mg images (logarithmic gray scale) with coronal hole boundaries and current-sheet projection (as in movie IIa) shown. The times of the nearest MDI and SXT full-disk images are also shown.

[a] CD-ROM movies also at *http://canopy.lmsal.com/~schryver/Sun/Field.html*

are contours of slightly smoothed bitmaps that show the end points of two sets of field lines that were found to connect the photosphere to the source surface (see Section 2). Such a mapping results in steady contours whenever an area has a substantial open flux; outward tracing of field lines allows us to determine accurate maps of large photospheric areas that have weak fields and relatively little flux reaching into the heliosphere, whereas inward tracing allows us to find compact photospheric sources of substantial heliospheric flux. Contours drawn around only one or very few widely-spaced footpoints of traced field lines, in contrast, tend to flicker or evolve rapidly. More detailed connectivity studies would likely result in smoother evolution, but that is beyond the scope of the present paper. Further rapid variations are caused by the incomplete assimilation of bipolar regions, as discussed in Section 3.3.

Despite the fact that in general individual active regions affect the overall properties of the heliospheric only mildly (see Section 3.4), the assimilation of some strong active regions can lead to substantial changes in ACH boundaries even half a solar radius away. Around 26 October 2001, a narrow, long ACH flickers into existence (in Movie IIa), but it is not until AR 9682 is assimilated that the ACH truly forms at the proper position to match an XCH channel of which only the northernmost part is apparently wide enough to allow a CCH to show up (in Movie III). For a few other examples, see Movie IIa around 18 October 2000, or the days prior to 23 April 2001.

The most stable ACHs, i.e., those with significant fluxes, correspond best with CCH and XCH structures. Hole boundaries in the He I 10830 Å maps (CCH) are to be compared to the ACH boundaries around central meridian passage, because they were determined near that time and do not evolve with time within a single rotation. Comparison of the three sets of coronal hole boundaries clearly reveals projection effects in which the 3D structure of the corona can mask part or all of the footprint of the coronal hole in the *Yohkoh*/SXT soft X-ray images, or can distort the outline of the coronal hole in the X-ray images by line-of-sight integration (particularly for narrow channels, see Movie IIa around 16 May 2000, for an example). Details of coronal hole boundaries may also depend on the data assimilation, which is complete only for regions well within 60° of disk center.

Some coronal holes live for a very long time, even those not very large, with flux drifting through them. These holes survive on flux fed in from fortuitously emerging active regions. A good example is a coronal hole with central meridian passage on 30 July 2000, at $\sin(\theta) \approx -0.5$. That patch can be followed, with only a few interruptions, all the time to the end of the data set on 30 December 2001, i.e., a duration of 17 months. The patch sometimes moves rapidly from one area to the next, after which it remains tied to a particular longitude temporarily, with its higher-latitude extension drifting over it in the differential rotation. For a time, the patch is part of another coronal hole, straddling the equator with central meridian passage on 16 September 2000. This larger hole illustrates how the hole and the flux within it can rotate at significantly different speeds; for an explanation of rotation properties of coronal holes we refer to Wang and Sheeley (1993).

3.3. Patterns in the interplanetary magnetic field

Figures 2–4 summarize the evolution of the heliospheric field at the source surface above the solar equator (i.e., within ±7° of the ecliptic, depending on the time of the year)[4]. The top rows in each of these figures shows the results for the simulation model M. These show that the equatorial source-surface field evolves smoothly, with typically either two or four sectors for the field polarity; periods in which there is a six-sector structure are few, and typically last no longer than a month.

[4]Compare with Wang and Sheeley (1995) for similar field polarity diagrams for the period of 1976 to 1994.

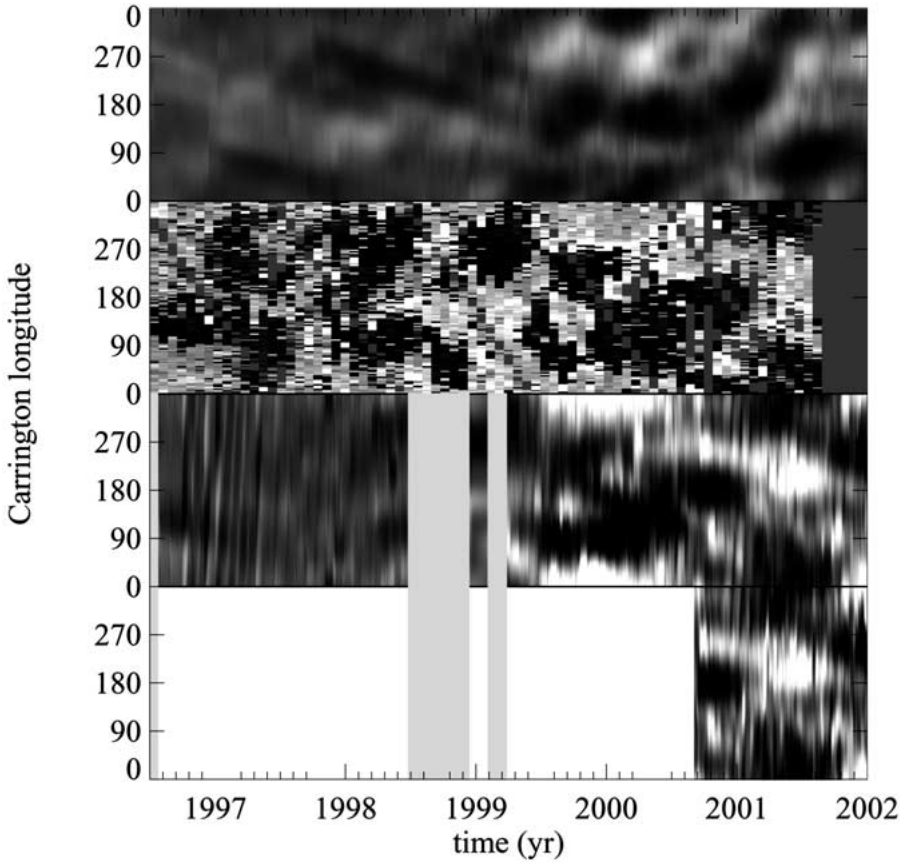

Figure 2. Gray-scale longitude–time diagram of the strength of the heliospheric field over the solar equator at the source surface at 2.5 $R_\odot$ (where it is a close approximation of the IMF). Each panel shows a vertical line for each 6-hr time step, that shows the field strength at the source surface. *Upper strip*: simulation model M of solar activity. *Second strip*: observed IMF at Earth (see text; neutral gray where no value is available – see right-hand edge). *Third strip*: model A based on assimilated MDI magnetograms. *Lower strip*: model A_f, which includes the assimilation of far-side acoustic images. Monopole corrections were applied as necessary.

The generally smooth evolution of the polarity and field-strength patterns in model M is solely a consequence of the fact that it is dominated by the largest-scale patterns in the surface magnetic field, which evolve slowly. The persistence of preferred longitudes for the IMF polarities, centered around 90° and 270° for several years, can apparently occur despite the fact that there are *no* longitudinal preferences for flux emergence or transport in this simulation model M.

We also point out that the sector boundaries are not very sensitive to the fact that active regions are injected instantaneously into simulation model M, rather than that they increase in strength gradually over a few days as observed for the real Sun: the effects of even a large active region, when just emerging, on the sector

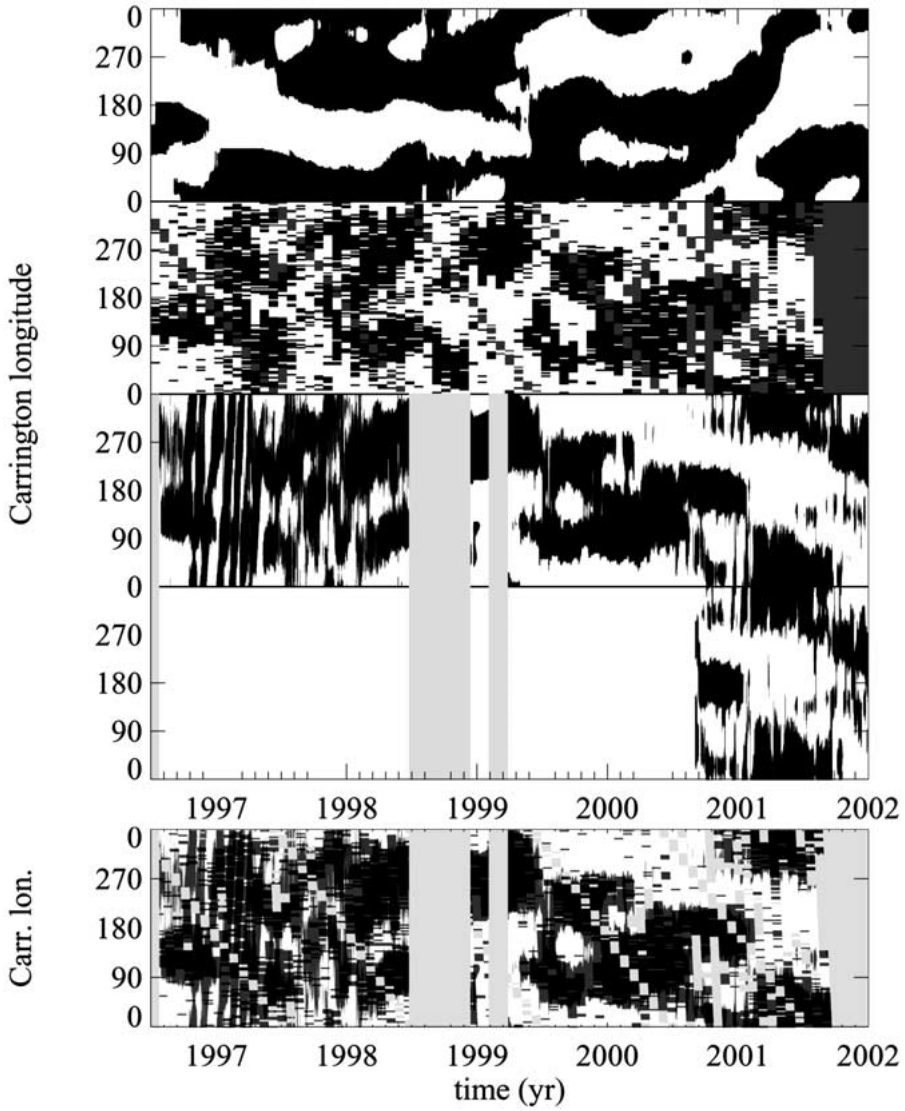

Figure 3. Top: longitude–time diagram of the polarity of the heliospheric field over the solar equator at the source surface at 2.5 $R_{\odot}$; see Figure 2 for a description of the layout. *Bottom:* comparison of computed and measured polarities of the interplanetary magnetic field in a longitude–time diagram. Where the values match, the image shows *black* or *white* to reflect the polarity. *Dark gray*: values do not match. *Light gray*: no IMF data or incomplete data for assimilation.

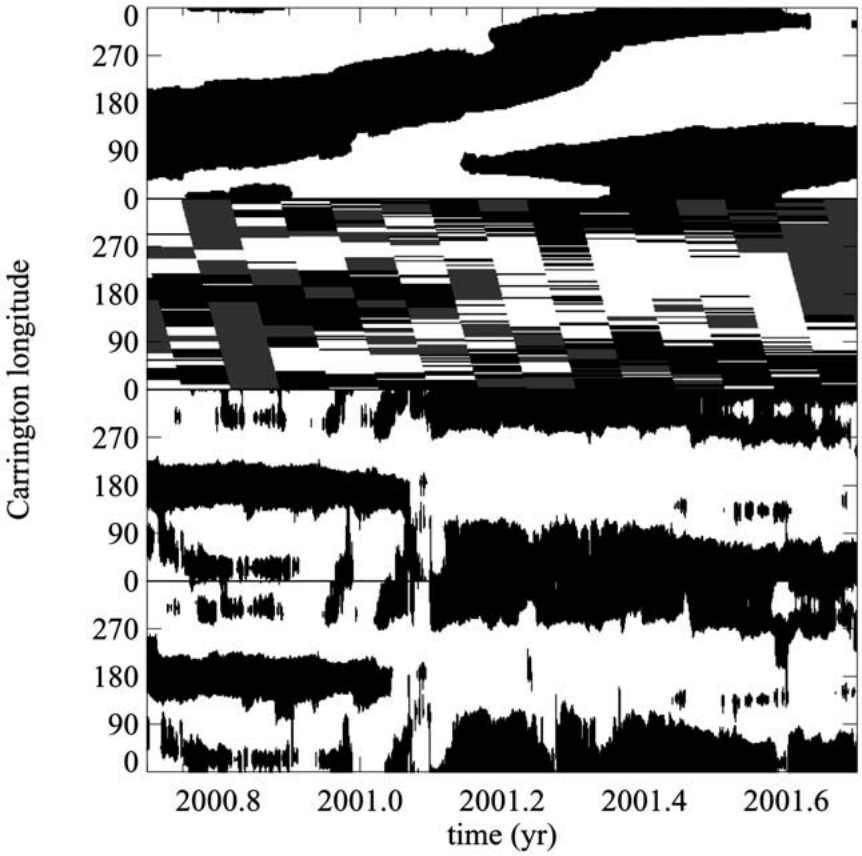

Figure 4. Detail of the top panel in Figure 3: longitude–time diagram of the polarity of the solar equatorial field at the source surface for 2000.7–2001.7 for model M, observed IMF at Earth, and for models A and A_f.

boundaries is at most a single resolution element (compare Figure 4) equivalent to just under 3°.

There is a marked contrast between the pure simulation model M and the data-assimilation models A and A_f (shown in the lower two rows of Figures 2–4). In the assimilation models, we find substantial short-term jitter in both the magnitude of the field and the polarity pattern. Mostly, this jitter is limited to one or two times the 3° resolution, but even that leads to a more ragged appearance of the IMF sector boundary diagrams than found for simulation model M. Frequently, however, the excursions are significantly larger, sometimes briefly reaching up to $\sim$ 45°, and sometimes leading to sector boundaries that survive for at most a few 6-hr time steps. As these short-lived excursions are much smaller in the simulation model M, we attribute the jitter in the computed heliospheric current sheet in model A to incomplete assimilation of bipolar regions straddling the eastern edge of the assimilation window. Each time a new or significantly-evolved magnetic bipole is

partly assimilated at the eastern edge of MDI's field of view, a flux imbalance is introduced into the model. Even though the corresponding monopole is removed prior to the computation of the heliospheric field, its presence remains noticeable. This monopole correction (employed similarly in other algorithms, such as that of the Wilcox Solar Observatory) essentially places a compensating monopole at the Sun's center, whereas the real culprit is located near the eastern edge of the assimilation window. That offset introduces a substantial dipole into the model that distorts the current sheet. Once most of the bipolar region is assimilated, this monopole correction vanishes again, and the sector-boundary structure returns to its proper, undistorted state.

The assimilation model contains diagonal bands in the polarity pattern of the equatorial source-surface field. These bands are visible from the middle of September 1996 through the middle of April 1997 in Figures 2 and 3, with a periodicity of approximately 26 d. This is likely an artefact associated with an imperfect zero-point level for the MDI magnetograms: even a weak latitude dependence in the instrument's zero point will be important at this phase of the cycle, because at that time the Sun's activity level is low and thus dominated by the weak signals, while the strong polar-cap fields that still exist at that time restrict the current sheet to be close to the equator. Hence, the IMF sector structure is particularly sensitive to small magnetogram errors in that phase of the cycle. As any detector-related artefact rotates eastward in the Carrington frame with solar rotation, a beat period of $\sim$ 26 d is readily introduced.

In order to test how well our model matches the real conditions in the heliosphere, we compare the modeled heliospheric magnetic field with measurements of the interplanetary magnetic field (IMF) near Earth as compiled in the OMNI-Web data base of the NSSDC at Goddard Space Flight Center[5]. We compare the computed field polarity at the source surface with that at Earth by determining the direction of the IMF relative to a line pointing 45° away from the Sun–Earth line in the direction of the Earth's orbital motion, which is the average angle of the IMF near Earth as it deforms in the Parker spiral from the source surface to the Earth orbit (e.g., Hundhausen, 1972). The comparison of model A and IMF measurements resulted in a best match if the Carrington longitudes at the time of the IMF measurement were shifted by 60° to compensate for the mapping between the field at the source surface and at the Earth's orbit in the Parker spiral. This optimal correlation corresponds to a time delay of 4.5 d, which reflects the average time it takes the solar wind to travel from the source surface to the Earth's orbit at an average wind speed of $\sim$ 400 km s^{-1} (that same delay was first reported by Ness and Wilcox, 1964). The result is shown in the second panels from the tops of Figures 2–4. Note that we have introduced a sliding horizontal offset to reflect that the near-Earth IMF is sampled only once per solar synodic rotation, and therefore in effect only on the leftmost edge of each slanted column.

[5]OMNIWeb URL: http://nssdc.gsfc.nasa.gov/omniweb/ow.html

The sector structure in the assimilation model A and the IMF data generally agree, as can be seen in the bottom panel of Figure 3. The comparison is particularly good from 1998 onward. For comparison, the computed and predicted polarities match 65% of the time up to the loss of SOHO in the summer of 1998. For the period after the spring of 1998, the results match the observations for 83% of the time. That match is quite good, in view of the relatively poor sampling of the sector structure by IMF measurements, the assumptions of a fixed wind speed and a simple Parker spiral for the field, the neglect of the b angle and of CME-related variability (responsible for many of the thin bars in the diagram of the IMF data), and equal weighting of all polarities regardless of the magnitude of the field. A similar comparison of the IMF polarities using potential-field extrapolations based on Wilcox Solar Observatory data[6] results in a match of polarities 68% of the time.

3.4. ASSIMILATION OF THE FAR-SIDE ACOUSTIC IMAGES

The helioseismic far-side data successfully identify large active regions that emerged prior to crossing the central meridian passing through the antipode of disk center (movie IIb). One of many examples is a series of active regions identified on the far side around 15 March 2001, mapping very well onto the front some ten days later. The far-side data are therefore very useful in forecasting, e.g., irradiance variations associated with large active regions, or potential sites of flares.

For the computation of the heliospheric field, in contrast, the far-side data make little difference. A comparison of movies IIa and IIb reveals that the details of the coronal hole boundaries and the current sheet differ somewhat between the two models, but there is no systematic difference by which we can favor one over the other. That impression is supported by a quantitative comparison with the IMF data: for the period 2000.7 through 2001.7 (best seen in Figure 4) the assimilation model A correctly identifies the polarity of the IMF 84% of the time, while inclusion of the far-side data in model A_f slightly lowers that success percentage by 1.4% (which may well be an insignificant difference).

It is perhaps not surprising that assimilation of the far-side data are of little consequence for the observed coronal hole geometry and the near-Earth IMF. At the time for which we make the comparison, the heliospheric field is dominated by a substantial number of active regions, both mature and decayed. Adding a few more compact regions on the other side of the sphere makes little difference for the coronal holes on the front, particularly when the large-scale (and thus long-range) flux patterns are well described by the front-side assimilation and subsequent evolution by the flux-transport processes.

[6]URL: http://quake.stanford.edu/~wso/Source.250.rad/

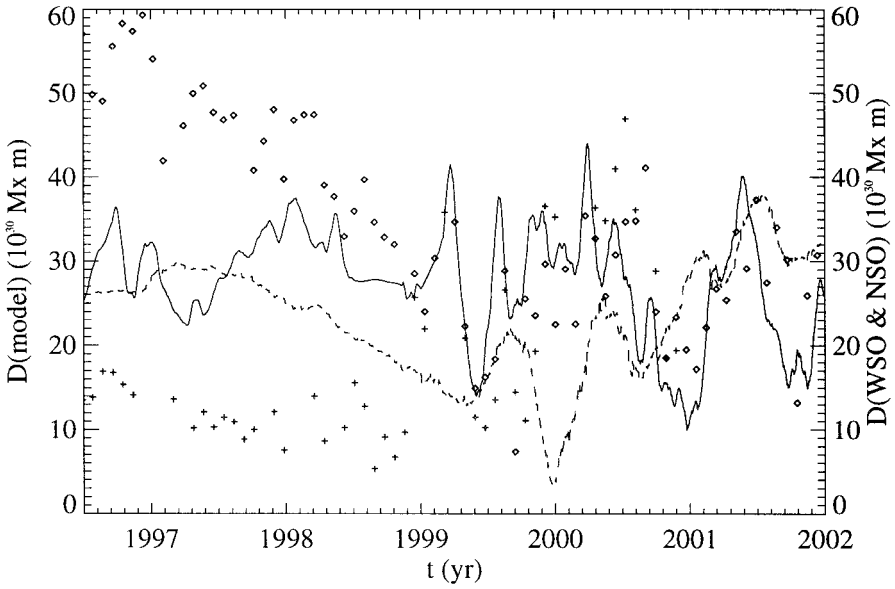

Figure 5. Magnitude of the global dipole moment for the assimilation model A (*solid*; boxcar averaged over two synodic solar rotation periods), compared to the results based on NSO (*diamonds*) and WSO (*pluses*) synoptic maps. No latitude-dependent correction factors were applied. The *dashed line* shows the dipole moment measured from the pure simulation model M.

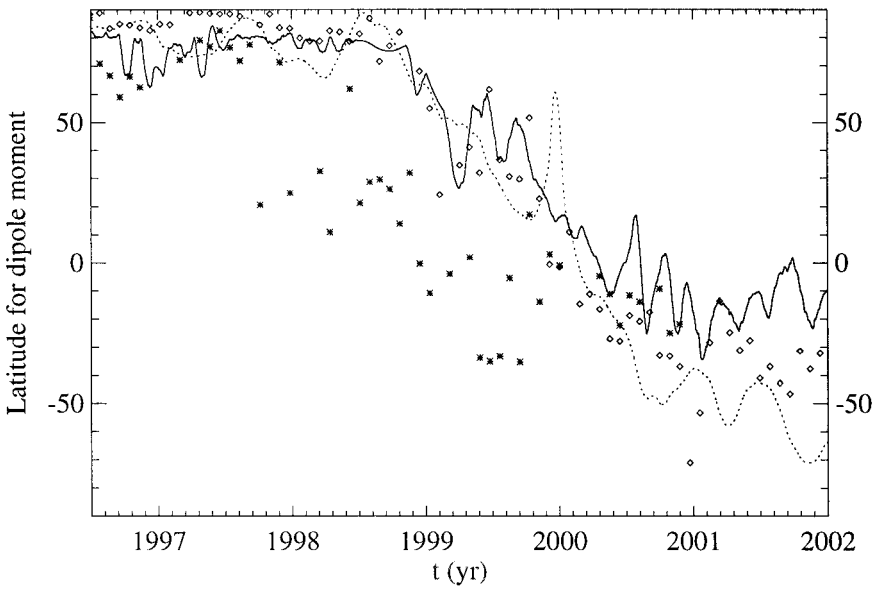

Figure 6. Tilt angle of the global dipole moment, shown as the equivalent latitude, for the assimilation model A (*solid*; boxcar averaged over two synodic solar rotation period), compared to the results based on NSO (*diamonds*) and WSO (*pluses*) synoptic maps. Similarly computed dipole tilt angles for a pure simulation model M are shown by the *dashed line*. No latitude-dependent correction factors were applied to the NSO and WSO data.

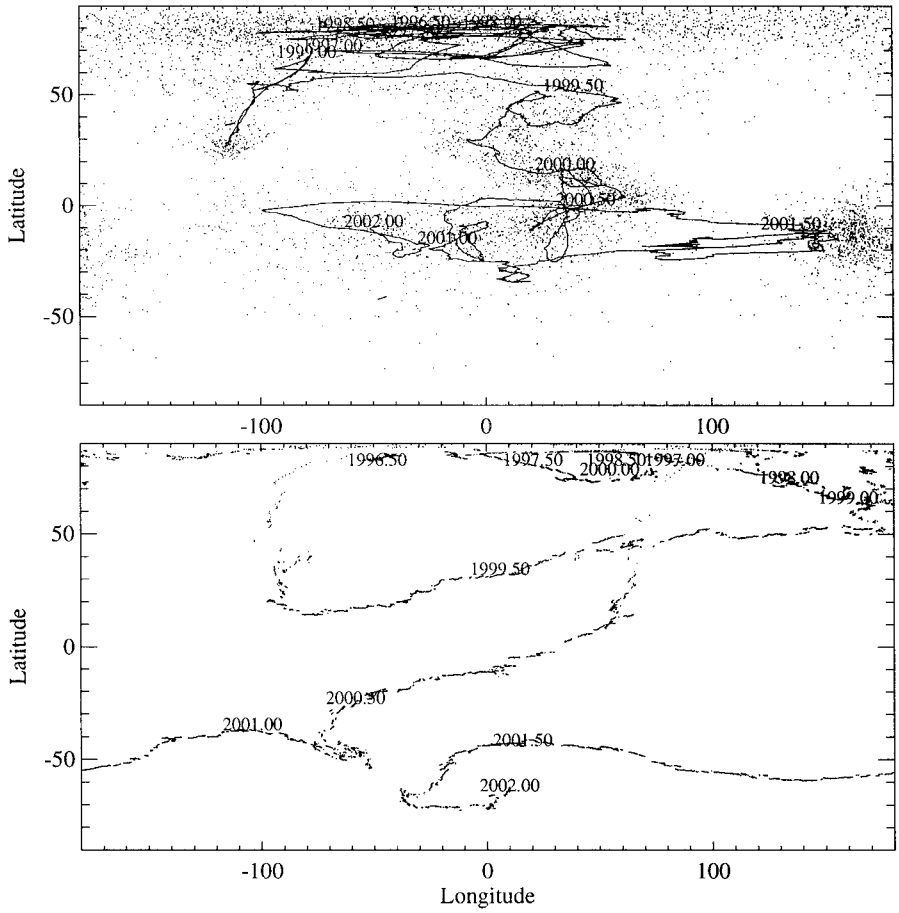

Figure 7. Latitude–longitude representations of the direction of the dipole component of the global solar field. *Top:* assimilation results (model A); *dots* show the instantaneous positions (at 6-hr resolution), while the *line* (with labels spaced by 6 months) shows the track after boxcar smoothing over four rotations. *Bottom:* simulation results (model M); *dots* show the instantaneous positions (at 6-hr resolution), with no smoothing applied.

4. The Global Dipole Moment

Figure 5 shows that the solar global dipole moment ranges over about a factor of 4, with a relative standard deviation of 29%, throughout the 5.5-yr period for which the assimilation is performed, but without a clear trend through the years from cycle minimum to maximum. This is compatible with the observations that the heliospheric field strength, although variable, shows relatively little change over the decades even as the solar photospheric flux density, for example, changes by a factor that reaches up to five, depending on the cycle (e.g., Wang and Sheeley, 1995; Wang, Lean, and Sheeley, 2000; Balogh and Smith, 2001; Schrijver, DeRosa, and Title, 2002).

The dipole moment measured for the assimilation model A for phases near cycle maximum is in fair agreement with estimates based on synoptic magnetic maps prepared at the Wilcox Solar Observatory[7] and at the National Solar Observatory, based on Kitt Peak Vacuum Telescope observations[8]. For phases near the cycle minimum, the differences between the assimilation model A and the two ground-based observatories are substantial. This is likely a consequence of the fact that in these phases the high-latitude fields dominate the dipole moment, and these fields are difficult to measure, often requiring substantial latitude-dependent correction factors (e.g., Wang and Sheeley, 1995). In comparison, the pure simulation model M (dashed line) has a dipole moment that is comparable to that of the assimilation model A during minimum and maximum, but with a minimum in between around 2000. This is a consequence of the decrease in polar-cap flux counteracted by an increase in active-region flux; that such a dip is absent in the assimilation model likely reflects the details of the phasing of one cycle relative to the next as well as the detailed cycle profiles.

The solar dipole moment gradually tilts away from alignment with the rotation axis from cycle minimum to maximum, starting towards the end of 1998 (Figure 6). The tilt angle for model A is in fair agreement with the NSO data up to the second half of 2001. In contrast, there is a substantial difference with the WSO data, which show an earlier, noisier decrease in the tilt angle (note that no latitude-dependent corrections were applied for these comparisons). We presume that this is due to the poorer resolution of the WSO instrument, which may cause a substantial underestimate of the polar field relative to the lower-latitude fields. In the present study, we do not investigate the origin of these discrepancies further. Instead, we point out the interesting agreement between the dipole tilt angles for models A and M until about the middle of 2000. At that time, solar activity picked up again, forming a double-peaked cycle in the sunspot number[9]. Such behavior is not included in the simulation model M, which uses an average cycle profile for the progression of the sunspot number. The difference between the observations and simulations is to be investigated further.

The remarkable agreement in the tilt angles for models A and M prior to the fall of 2000 suggests that the observed gradual tilting of the solar dipole moment requires no particular properties of the dynamo or of the surface transport: the gradual tilting in model M results without preferential longitudes or active-region properties.

For completeness, we show the trajectories of the dipole moment in latitude and longitude for the two models in Figure 7. The direction of the vector for the assimilation model A is much noisier than in simulation model M; this is largely attributable to the incomplete assimilation of bipolar regions at the eastern edge of

[7]URL: http://quake.Stanford.EDU:80/~wso/Photo/
[8]URL: ftp://argo.tuc.noao.edu/kpvt/synoptic
[9]URL: http://www.sel.noaa.gov/SolarCycle/

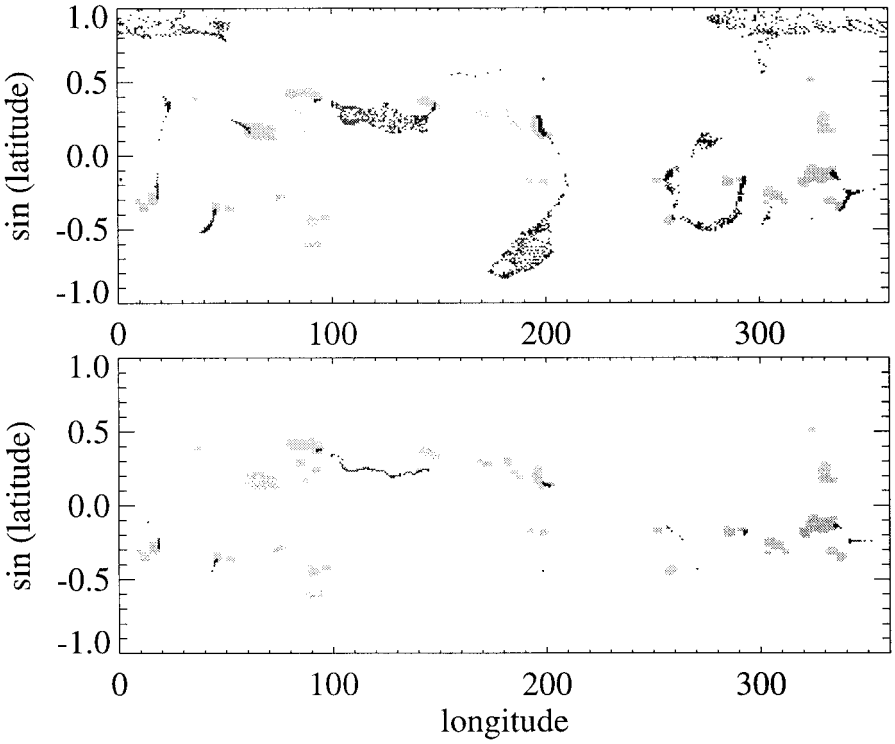

Figure 8. Maps $(\sin(\theta) - \phi)$ of the origins of the global heliospheric field (*top*) and of the equatorial heliospheric field (*bottom*) for 13 March 2001 (compare Figure 1). The *dark dots* show the photospheric footpoints of 2356 and 360 field lines, respectively, traced inward from the source surface. The *gray patches* identify regions with absolute flux densities exceeding 50 Mx cm^{-2} at a resolution equivalent to 1° at the equator, including pixels immediately adjacent to these regions.

the MDI assimilation window combined with the simple monopole correction that is applied.

5. Sources of the Heliospheric Field

Inspection of field-line footpoints (such as marked in Movies IIa and b; see also the example of field-line footpoint maps in Figure 8) confirms that much of the heliospheric field has its origin in well-defined, large coronal holes including those covering the polar caps around cycle minima, and in narrow coronal channels and relatively small patches in the quiet network. It also reveals that much of that field originates in the magnetic plages of active regions. Almost all field lines that we find to connect the heliosphere to a magnetic plage start from regions near the perimeter of plage that generally continue into unipolar network.

In order to quantify how much of the heliospheric flux originates from different source regions within the photosphere, we differentiate between four types of regions:

(1) the polar caps poleward of 60°,

(2) the mid-latitude regions above the activity belt, i.e., 30–60°,

(3) the magnetic plage areas (defined as areas with a flux density exceeding 50 Mx cm^{-2} on a $\sin(\phi) - \theta$ synoptic map with a resolution of 1° at the equator, plus pixels immediately adjacent to these) between ±30°, and

(4) the non-plage activity belt between ±30°.

The fraction of the source surface connected to each of these types of regions was determined by locating the end points of a set of field lines traced inward to the photosphere from a set of uniformly distributed points on the source surface (2356 lines in each case, corresponding to a spacing of 2 heliocentric degrees at the source surface). The results are summarized in Figures 9 and 10. Note that because the field strength at the source surface exhibits only a relatively weak variation from position to position, the fraction of the field lines ending in each type of area is a good approximation to the fraction of the heliospheric flux. The sampling from equidistant points on the source surface is more relevant to heliospheric studies, however, because the high-β plasma essentially moves out mostly radially from that surface, so that our sampling scheme reveals the fraction of the total solid angle filled with wind from the different source regions.

We find that at cycle minimum, ∼ 70% of the heliospheric field lines originate from regions poleward of 60°. Not surprisingly, this decreases to the order of one percent around the time that the polar cap reverses polarity. An additional 10–20% of the heliospheric flux originates from the belt between 30° and 60° in latitude. That fraction roughly doubles from cycle minimum to maximum. This component dominates the polar component after the middle of 1999.

As activity increases, the fraction of the field originating in the activity belt (±30°) increases from 15% at cycle minimum to 70% or more after the beginning of 1999 around cycle maximum. Most of that flux originates from decaying active regions or unipolar areas in the quiet Sun, but starting around the spring of 1999, on average ∼ 20% of the traced heliospheric field lines end in what corresponds to mature, strong active regions. The latter fraction can at times reach up to ∼ 40%.

The fraction of the solar surface from which the heliospheric field originates is, as already mentioned in the Introduction, very small, because the field is bunched in small concentrations of high field strength. We now examine the locations of those regions of the solar surface from where flux concentrations connect to the heliosphere. We determine this based on the resolution of the standard synoptic map, i.e., with equal-area pixels and a resolution of one square degree at the equator. We then determine the fraction of all resolution elements that contain at least one end point of the set of field lines traced inward from the heliosphere. Figure 11 shows that the fractional area connected to the heliosphere decreases from 20–30% (average 22%) at cycle minimum, largely covering the mid-latitude regions, to

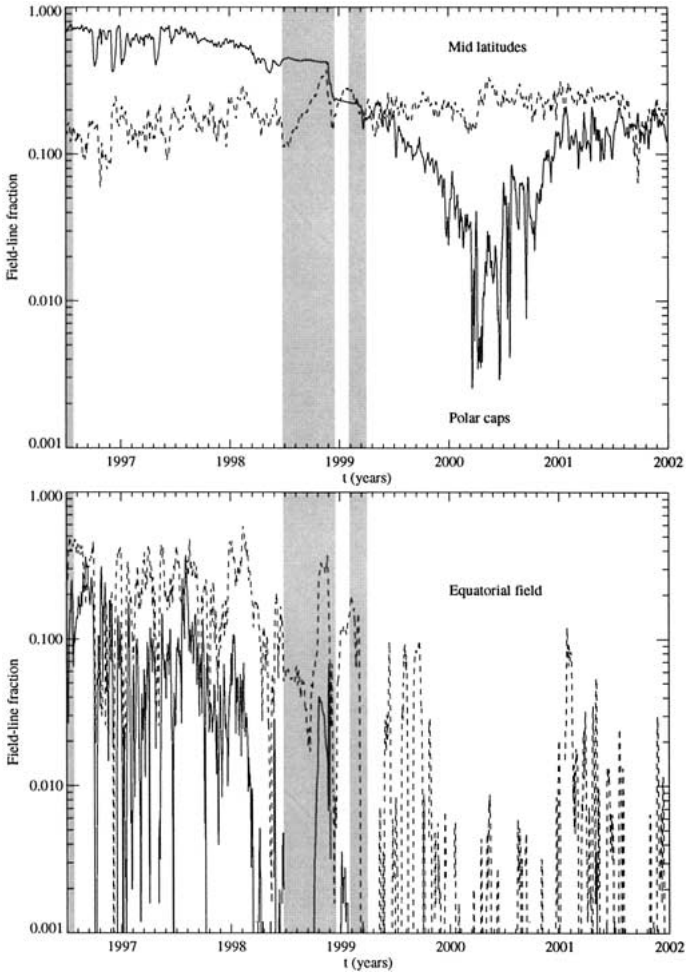

Figure 9. Top: fraction of the heliospheric field lines originating in the polar caps (poleward of 60°; *solid*), and in the mid-latitude range (30°–60°; *dashed*). The data were smoothed with a 3-day boxcar filter. Extended intervals for which no magnetograms were assimilated into the model are *shaded*, including the subsequent full solar rotation during which assimilation is incomplete; the initial rotation following the start of the assimilation procedure is also shaded. *Bottom:* as the top panel, but for field lines starting at the equatorial plane on the source surface.

10–20% (average 13%) of the area at cycle maximum, then largely originating from low latitudes.

The fraction f_O of the surface area covered by open field for cycle minimum of around 20% agrees with the observed coronal hole coverage inferred from *Skylab* soft X-ray observations for the cycle decay phase in 1973 (Levine *et al.*, 1977), as well as model values for the minimum around 1986 and the early rise phase of the cycle in 1976 (Wang and Sheeley, 1992). In contrast, the characteristic minimal values of f_O for phases just prior to maxima found by Wang and Sheeley

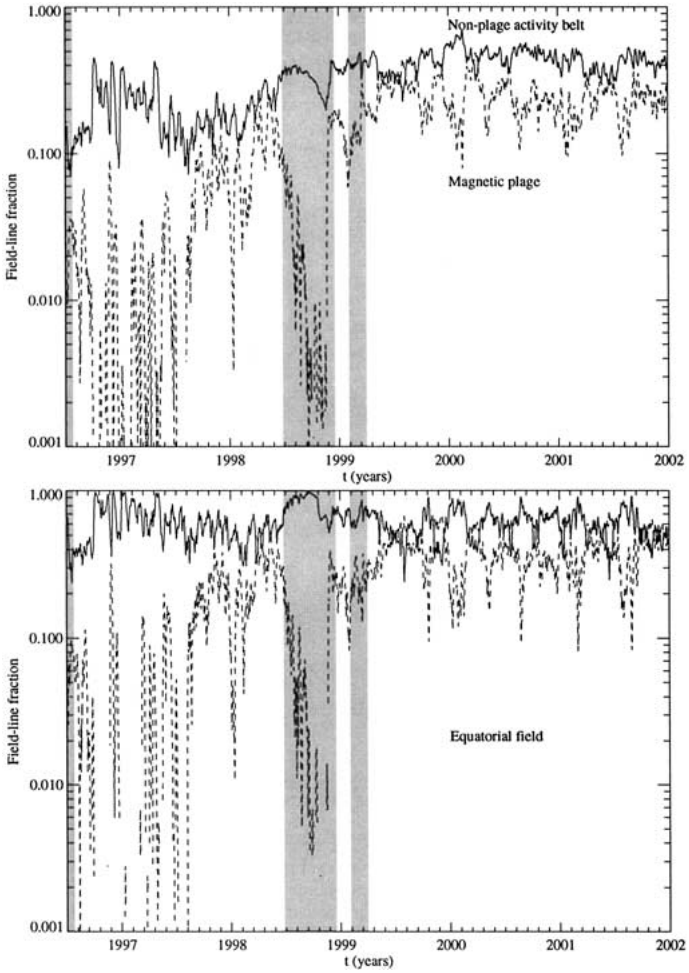

Figure 10. Top: fraction of the heliospheric field lines originating in the activity belt (±30°) outside of magnetic plages (*solid*), compared to the fraction originating within magnetic plages (*dashed*), defined as areas with flux densities exceeding 50 Mx cm^{-2}, or within a pixel from these, at the resolution of the synoptic maps (1° at disk center). The data were smoothed with a 3-day boxcar filter. *Shaded bands* as in Figure 9. *Bottom:* same, but for the field lines in the equatorial plane at the source surface.

(1992) average around 8%, whereas we find a relatively constant value averaging approximately 12%. It remains unclear whether the latter difference is related to the particular cycle or is a consequence of model differences; perhaps our higher density of field lines that are traced inward from the source surface allows us to better trace large areas with low net flux densities.

The heliospheric field lines originating directly in magnetic plages, emanate from 5–10% of the plage area (lower panel of Figure 11). This number is remarkably constant throughout the 5.5-yr time series; note that the strong fluctuations

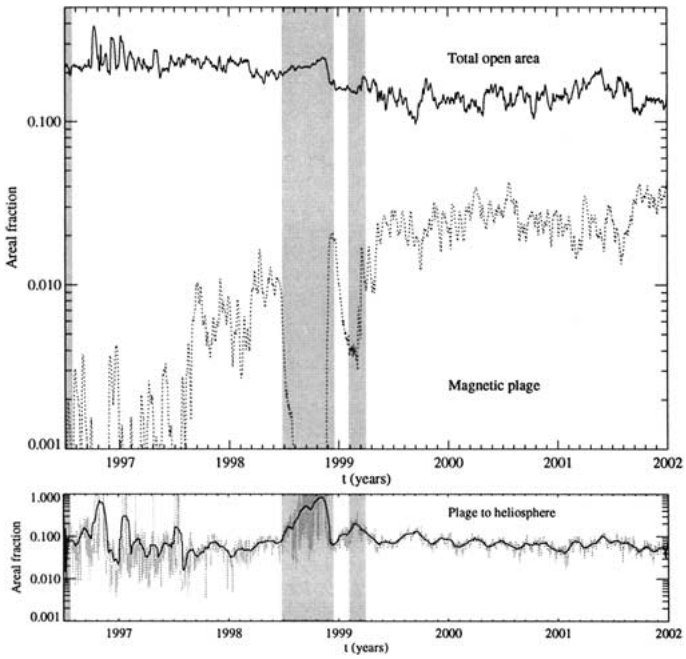

Figure 11. Top: fraction of the solar surface that is connected to the heliosphere (*solid line*), determined for a resolution matching that of the synoptic maps, i.e., with 1° on the equator. The fraction of the area filled with magnetic plage (with flux densities in the synoptic map exceeding 50 Mx cm^{-2} and pixels adjacent to these) is shown by the *dotted line*. The data were smoothed with a 3-day boxcar filter. *Bottom:* the fraction of plage pixels with at least one field line extending into the heliosphere, smoothed by one synodic rotation period (*solid*) and at full temporal resolution (*dark gray*). *Shaded bands* as in Figure 9.

late in 1996 and early in 1997 may be associated with the instrumental artefacts discussed in Section 3.3. The area of the solar surface that is, in turn, covered with magnetic plages reaches no higher than 2–4% at cycle maximum (upper panel of Figure 11).

6. Sources of the Interplanetary Magnetic Field

If we ignore the slight *b*-angle variation associated with the 7° tilt between the solar equator and the ecliptic, then field lines starting at the source surface over the solar equator can be used to quantify the origins of the interplanetary magnetic field that determines space weather conditions around Earth. The lower panels in Figures 9 and 10 show the sources of the equatorial field for the same four types of source regions as discussed for the entire heliospheric field in the preceding section. During cycle minimum conditions, some 20–40% of the field lines originate in the mid-latitude and polar regions, with the polar field contribution being both smaller and more variable. Around cycle maximum, Earth apparently sees no significant

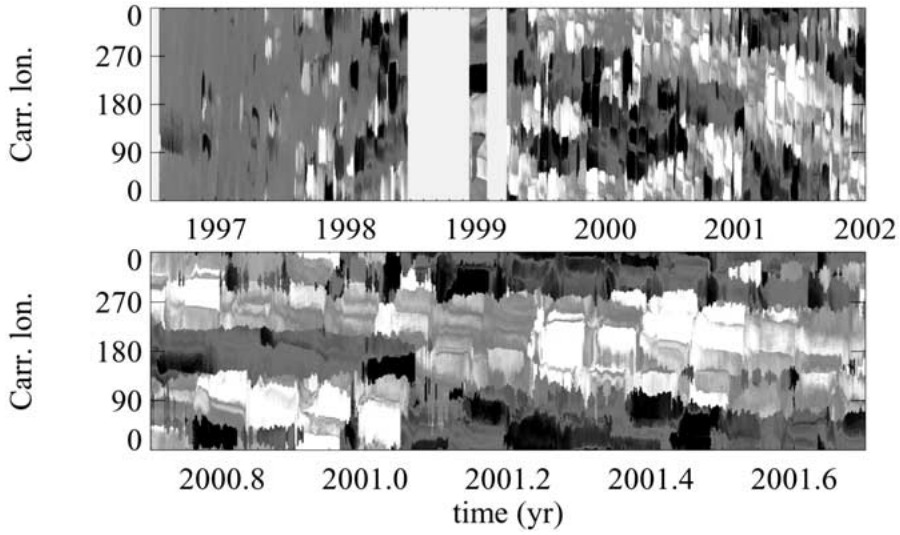

Figure 12. Flux densities at the photosphere of the end points of field lines traced from the equatorial plane at the source surface in a sin(longitude)–time diagram. *Top:* full time series. *Bottom:* time interval 2000.7–2001.7. The gray scale saturates at ± 300 Mx cm^{-2} at a resolution equivalent to 3° at the equator.

polar contribution, and the mid-latitude contribution is very intermittent, and rarely exceeds even one percent. In these phases, essentially all field lines in the equatorial plane originate in the activity belt, with on average 30–40% coming from magnetic plage.

Figure 12 shows, in the same format as the panels in Figures 2 and 3, the flux density at the photosphere for a resolution of 3° of field lines starting from the intersection of the equatorial plane and the source surface. The banded structure reflects the importance of active-region birth and rejuvenation on the invisible half of the solar surface: on each rotation, the field-line mapping and the flux densities in the photosphere can change significantly. The lower panel shows in some detail that the source regions for the ecliptic heliospheric field often differ substantially from longitude to longitude. We find that despite the deceptively simple polarity structure of the quiescent solar wind near Earth, the interplanetary magnetic field maps back to of order a dozen significant source regions on the Sun (grouped into polarity clusters that match the sector structure of the IMF polarity), with roots either in or near magnetic plages, or in weaker, large-scale unipolar regions. This mapping is scanned by (instruments near) the Earth as it orbits backwards about once per month in the reference frame of the rotating Sun; this leads to substantially more variability in the observed wind and IMF properties than expected from the evolution of the field itself when seen in the solar inertial frame shown in the movies. For one thing, the speed of the solar wind is inversely correlated with the expansion of the magnetic field from the source region to the heliospheric field

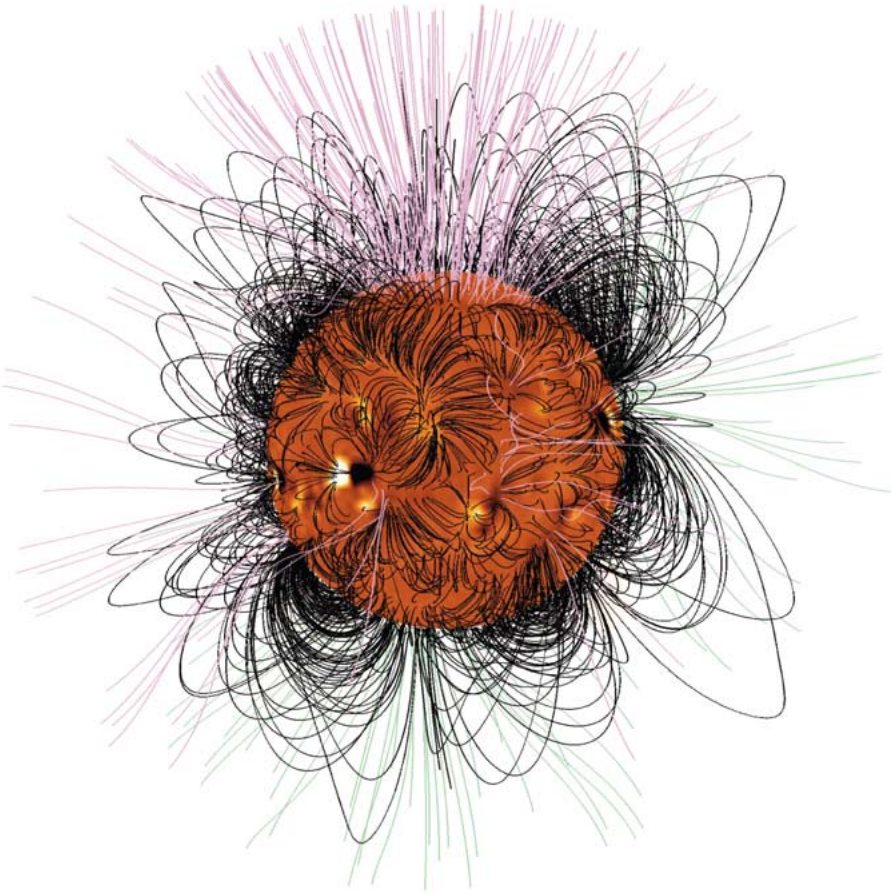

Figure 13. Low-resolution equivalent of a full-disk magnetogram, with computed field lines overlayed: *black* for closed field lines, *green* and *pink* for open field lines for field pointing away from or towards the Sun, respectively. The computed field lines start from a set of uniformly distributed points on the solar surface. Field from AR 9373 southeast from disk center (compare Figure 1) maps directly into the heliosphere, expanding rapidly with height. Comparison with Figure 1 shows that the open field lines from AR 9373 likely map into the leading spot.

(e.g., Levine *et al.*, 1977; Wang and Sheeley, 1990a). The mixture of quiet and active regions in which the IMF has its origins, with sharp transitions from one source type to the other, is likely also related to observed variability in the chemical composition of the solar wind (e.g., Von Steiger *et al.*, 2000).

7. Examples of Active Regions Connected to the Heliosphere

We examine the direct connection of much of the heliospheric flux, and even more of the interplanetary flux, to magnetic plages found in the modeling in two case

studies in which we compare high-resolution TRACE images of the EUV corona to full-resolution magnetograms and the field configurations determined with the source-surface model.

The first case is illustrated in Figures 1(d–g); these show a TRACE 171 Å image (see Handy *et al.*, 1999, for a description of TRACE) of the active-region complex formed by NOAA ARs 9373, 9374, and 9380 next to, as well as blended with, the MDI magnetogram. The full-sphere magnetic field configuration for the corresponding time is shown in Figure 13, and a cutout of that in Figure 1(g).

The source-surface potential-field model matches the general configuration of the field traced by EUV-bright loops quite well. The field extrapolation shows that the westernmost area of AR 9373, in which almost all flux is contained in the leading spot, should be connected directly to the heliosphere. TRACE, which observed this region continuously from 13–21 March 2001, shows that there are no bright loops emanating from the westernmost side of the leading spot, which is otherwise commonly seen around sunspots (e.g., Schrijver *et al.*, 1999). It is unlikely that these missing loops emit at a significantly different temperature, because spot loops are in general not seen in soft X rays (e.g., Sheeley *et al.*, 1975), i.e., at temperatures above the 1 MK range that is imaged by TRACE's 171 Å pass band. Hence, the TRACE observations are compatible with the field model that (part of) the sunspot flux is open. In addition, the volume from which EUV-bright loops (and X-ray bright loops; see Figure 1(c), or Movie III) are absent matches the volume where field lines are modeled to be open quite well. The correspondence of a region where field is computed to be open to the heliosphere with a dark coronal region where in other circumstances bright loops are expected is strong support for the direct connection of the heliosphere to this plage. In this case, where there is very little flux westward of the leading spot, the sunspot itself must directly connect to the heliosphere.

Another case study of an active-region source for heliospheric flux is shown in Figure 14 for NOAA active region 8525. Our model shows both plage flux and spot flux to be open into the heliosphere. As there is leading-polarity flux westward of the sunspot, associated with a dark patch in the *Yohkoh*/SXT image in Figure 14(b), this case is not unambiguous about the connection from spot to heliosphere, but the TRACE and *Yohkoh*/SXT observations do suggest that plage flux reaches into the heliosphere as inferred for a potential-field configuration.

Note that for the two days following the images shown in Figure 1 and for six days around those in Figure 14 (see Movies IIa and III), the subsolar point on the source surface (indicated by the large diamonds in Figures 14(a) and 14(b)), resides within the open-field areas associated with these regions: this means that the solar wind that reaches Earth 4–5 days after it leaves the Sun originated directly from plage and sunspot fields.

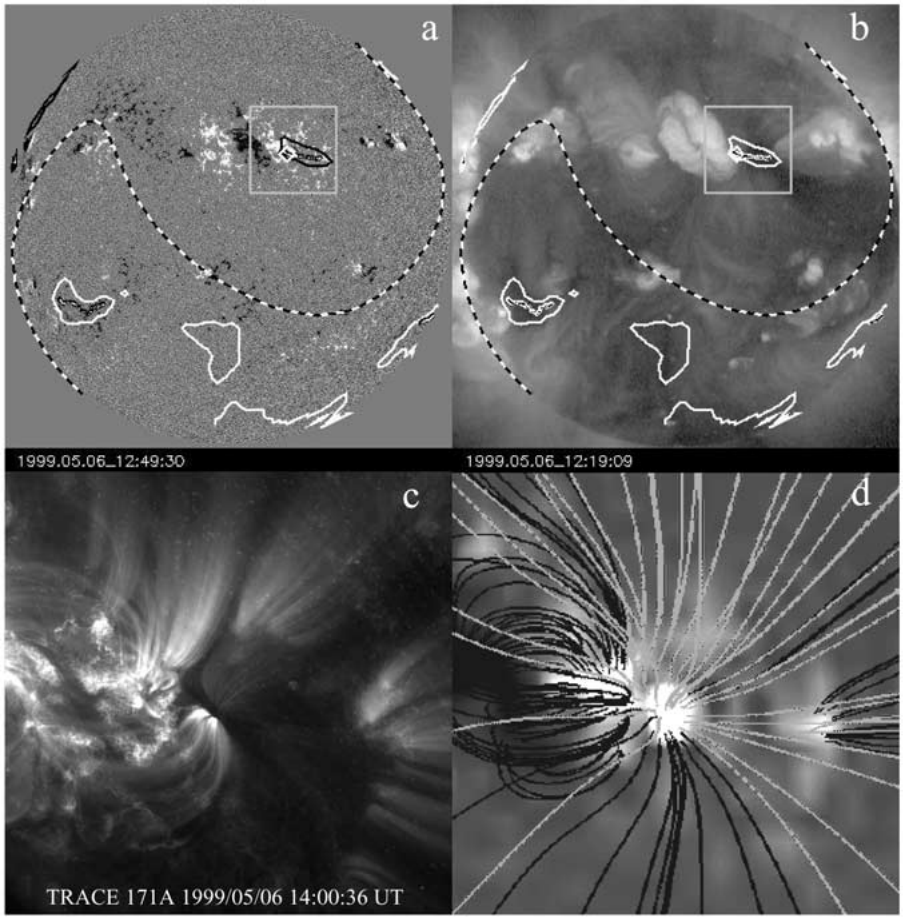

Figure 14. Example a direct connection between the heliospheric field and the field in the magnetic plage around the leading spot, and likely the spot itself, of active region 8525. The *gray square* in panels (a) MDI magnetogram and (b) SXT X-ray image corresponds to the field of view in (c) TRACE 171 Å and (d) field extrapolation: closed field lines are *dark gray*, open field lines *light gray*. The caption to Figure 1 describes the curves and other features in (a) and (b).

8. Discussion and Conclusions

We develop and test a flux-dispersal model for the solar photospheric magnetic field, based on a model with data assimilation. The model, with standard differential rotation, meridional flow, and supergranular diffusion, shows no significant differences between model and observation upon the return of regions to the observable near side of the Sun, to an accuracy of order a degree (and barring rejuvenated nests of activity). We therefore conclude that the flux-dependent coefficient for random-walk dispersal of field, a rotation profile tuned to that of young activity nests, and the description of field transport by the equivalent surface-transport of

a signed scalar field adequately approximate solar conditions for the purpose of full-sphere field modeling.

We use this model of the surface magnetic field as the boundary condition for a source-surface potential-field approximation of the high corona and inner heliosphere for a quantitative study of the origins of heliospheric field. The mapping of the heliospheric field to its origins on the solar surface has been the subject of numerous earlier studies. This study adds to that knowledge by (1) demonstrating that the combined flux-dispersal and source-surface heliospheric modeling works well for not merely a few select examples, but for a continuous data set spanning a 5.5-yr interval from the most recent cycle minimum to past cycle maximum at 6-hr resolution, and (2) providing a quantitative breakdown of the photospheric sources of the heliospheric field for that entire period.

Although it is known that heliospheric flux can map back to areas near or in magnetic plages (e.g., Levine *et al.*, 1977; Levine, 1982),[10] we find that such connections are common, and that these are responsible for up to about half of the flux in the interplanetary magnetic field (IMF) during cycle maximum (that estimate does not include the contribution by field involved in dynamically evolving transient coronal holes; e.g., Kahler and Hudson, 2001). We discuss two case studies in which the IMF likely emanates directly from sunspots.

The active-region sources of heliospheric flux described here are not occasional openings of the tops of active-region loops (which are not allowed by the model adopted), but rather long-lived (albeit evolving) connections from one side of active regions (depending on the location of the active region relative to the heliospheric current sheet). A matching amount of flux from the other side of the active regions is, of course, necessarily connected to other regions on the surface. Only in cases like coronal mass ejections would both polarities of the photospheric active region temporarily open up into the heliosphere.

[10] After submission of this manuscript, we learned about a parallel study by Neugebauer *et al.* (2002), entitled 'Sources of the Solar Wind at Solar Activity Maximum'. They combine source-surface modeling with 'ballistic' tracing of plasma trajectories through the heliosphere to the ACE and *Ulysses* spacecraft for the period of 1998 to 2001. For a subset of four solar rotations selected for their good agreement between measured and modeled polarities, they find – as we do – that active-region fields contribute substantially to the modeled heliospheric flux. They corroborate that finding by pointing out that the boundaries of adjacent plasma flows from different source regions (even if of the same polarity) are recognizable as magnetic holes, plasma sheets, and low-entropy intervals; active-region wind streams are otherwise only distinguished from coronal-hole streams by their higher O^{7+}/O^{6+} ion ratio. Based on this study, they suggest that 'there is perhaps a hierarchy of open field regions, with the large, polar coronal holes with very fast wind and very low inonization temperatures at one extreme, smaller, low-latitude coronal holes in the middle, and open, coronal-hole-like regions in a single polarity side of active regions at the other extreme'. We also learned about a recent study by Wang and Sheeley (2002), who also argue that active regions are sources of heliospheric flux, even shortly after their emergence. And finally, Luhmann *et al.* (2002) show maps of the flux densities at the footpoints of modeled heliospheric field lines that show that much of the heliospheric field near cycle maximum originates from regions with flux densities exceeding 30 Mx cm^{-2} at 5° resolution.

The field through the source surface above the solar equator is a good proxy for the interplanetary magnetic field. This field is demonstrated to map to of order a dozen disjoint domains on the solar surface during active phases. The marked differences in the properties of the source regions from one domain to the next are likely associated with substantial differences in bulk wind properties (speed, temperature, . . .) as well as in its chemical composition (related to the fractionation as a function of the first ionization potential, e.g., Von Steiger, Geiss, and Gloeckler, 1997).

The use of these evolving, full-sphere magnetic maps allows accurate reconstruction of the IMF polarity structure for 60–85% of the time (improving with activity level), even if no allowance is made for wind-speed variations and stream-stream interactions. Incorporation of far-side helioseismic information on strong active regions makes little difference in this success rate; such far-side information is likely of more importance in forecasting irradiance variations or eruptive activity, or when the heliospheric field is to be computed for other longitudes or latitudes than that of the Earth's subsolar point.

In parallel to the data assimilation model, we ran a pure simulation in which active regions are injected based on random selection from parent distribution functions based on solar observations. These two models are in remarkable agreement about the temporal behavior of the sector structure of the IMF, about the characteristic magnitude and temporal behavior of the heliospheric field, and even about such global properties as the tilt angle of the Sun's large-scale dipole. We conclude from this that no subtle flux-emergence patterns or field-dispersal properties are required of the solar dynamo beyond those that are included in the model in order to understand the large-scale solar and heliospheric fields (confirming earlier findings by Wang and Sheeley, 1990b, and Sheeley, Wang, and Nash, 1992).

Acknowledgements

We thank P. Scherrer for providing the far-side helioseismic data of SOHO's Michelson Doppler Imager, G. Slater for providing the set of *Yohkoh*/SXT images, S. Freeland for his help with SolarSoft and retrieving data sets, C. Heck for keeping all our processors running smoothly, and J. Harvey, A. Title, and the referee for comments on the manuscript as well as pointers to relevant literature. This work was supported by NASA/LWS grant NAG5-10832, TRACE contract NAS5-38099 with NASA Goddard Space Flight Center, and MDI-SOI contract NAS5-30386 with NASA through Stanford contract PR 9162. The NSO/Kitt Peak data used in this study are produced cooperatively by NSF's NOAO, NASA's GSFC, and NOAA's SEL. The He I 10830 Å coronal hole boundaries were made available by Karen Harvey and Frank Recely. The Space Environment Center (SEC) is part of the National Oceanic and Atmospheric Administration (NOAA). The National

Solar Observatory is operated by the Association of Universities for Research in Astronomy under a cooperative agreement with the National Science Foundation.

Appendix A. The Flux-Dispersal Model

In this study, we use a recently developed model of solar surface activity (Schrijver, 2001; Schrijver and Title, 2001). This model is an extension of the traditional surface-diffusion model (DeVore *et al.*, 1985; Wang and Sheeley, 1991; Wang, Lean, and Sheeley, 2000) and incorporates all of the ingredients that have been demonstrated to play a role thus far: flux emergence, random-walk dispersal, meridional advection, differential rotation, and removal of flux via cancellation. Rather than describing the photospheric field as a continuous medium evolving on a grid, our model tracks flux as discrete point sources. These sources coagulate or cancel with neighboring flux elements upon reaching a minimum separation, and fragment into smaller sources with a likelihood that depends on their flux. Our model incorporates ephemeral regions in addition to the active regions, and incorporates an approximation to the magneto-convective coupling that causes a tendency for concentrations to disperse increasingly more slowly with increasing flux. The model was demonstrated to accurately reproduce both geometric and quantitative properties of the last sunspot cycles (Schrijver, 2001), including the polar regions (Schrijver and Title, 2001; Schrijver, DeRosa, and Title, 2002).

One key difference between our simulation model M and the traditional surface-diffusion model by Wang, Sheeley, and colleagues, is that bipolar regions are not placed on the surface as observed, but instead are selected at random from distributions that approximate observed histograms of latitude, size, and orientation of magnetic regions as a function of cycle phase. As a result, we can simulate historical solar activity using records of sunspot counts to modulate the level of activity (as in Schrijver, DeRosa, and Title, 2002). For the simulation model M, yearly sunspot numbers were taken from the Solar Influences Data Analysis Center of the Royal Observatory of Belgium[11], complemented after 2000.5 with predicted values then available at the NOAA Space Environment Center[12].

We assign alternating polarities to the cycles, and allow for the fact that while one sunspot cycle is fading out near the equator, the next cycle has already started at higher latitudes (Wilson *et al.*, 1988).

In our model, we approximate the frequency with which bipolar regions emerge onto the surface as proportional to the observed sunspot number. The drift of the mean latitude of active region emergence is matched to the approximate duration of the past and present cycles. We do not modify the drift with latitude other than to match the cycle duration. The processes that transport flux following its emergence onto the surface are approximated in our model as time-invariant.

[11] URL: http://sidc.oma.be/DATA/yearssn.dat
[12] URL: http://www.sel.noaa.gov/SolarCycle/

At each time step, we check for collisions between concentrations to determine flux cancellation and coagulation.

An earlier study of the high-latitude and heliospheric fields over several centuries (Schrijver, DeRosa, and Title, 2002) revealed that a key ingredient was missing from this kind of modeling: if only advection by large-scale surface flows and dispersal are included in a model to describe the photospheric field, then intervals are found in which the polar-cap field does not reverse. As this was found in particular for the well-observed reversal around 2000, options were explored to bring the model into line with observations. Schrijver, DeRosa, and Title (2002) argue that an exponential decay of flux with a time scale equivalent to a half life of 5 yr removes the above problem, and is in overall agreement with observational records. Although this hypothetical decay needs interpretation and comparison to other options, we chose to include this process in our current modeling to allow direct comparison to our earlier studies; its importance for the 5.5-yr period studied here is limited. The initial condition chosen for our modeling also incorporates the 5.5-yr half life.

Appendix B. Data-Assimilation Procedure

SOHO/MDI magnetograms are assimilated into models A and A_f only for periods of zero roll angle, and only if the magnetogram is complete, and the standard deviation of the signal on two mid-latitude strips lies within 5σ of the average, and if the ratio of total positive and negative fluxes lies between $\frac{1}{3}$ and 3.

We apply the standard SOHO/MDI calibration, but subsequently divide fluxes by 0.6 to correct for the relative insensitivity of the filter-based, moderate-resolution SOHO/MDI magnetograph relative to spectrographic, high-resolution observations with the Advanced Stokes Polarimeter (see Berger and Lites, 2002, also for the MDI calibration procedure).

After re-binning the magnetogram into a 256×256 array, all pixels within 60° of disk center are identified, and the position and signal strength for each such pixel determined. Detector coordinates are then transformed to heliocentric coordinates (latitude and Carrington longitude) by correcting for the distance of SOHO to the Sun and the apparent b angle appropriate for the spacecraft's orbit (both provided in the FITS header of the files).

These pixels are then entered in the list of concentrations in the model, correcting for line-of-sight effects by assuming the field to be vertical to the solar surface. All concentrations that exist in the model's list within that same area are removed.

Once pixels leave the assimilation oval, or if no MDI magnetogram exists on a subsequent time step, the model will coagulate flux into concentrations that are no closer than 4200 km apart (see Schrijver, 2001). That results is a distribution of fluxes that converges to that found for the non-assimilated part of the solar surface generally within a few time steps. This method avoids the problems associated with

object recognition codes (thresholds, noise treatment, etc.). Most importantly, it requires no correction for flux that is not included in objects by the object recognition code (e.g., Hagenaar *et al.*, 1999) and it does not form clusters of very high flux for sunspot environments (which subsequently decay and move too slowly to be compatible with observations; see the description by Schrijver, 2001).

The inclusion of active regions based on far-side acoustic maps in model A_f requires object recognition and calibration. Objects in the far-side maps are defined by identifying contiguous areas of pixels on the $\sin(\theta) - \phi$ grids that exceed a threshold $\mathcal{T}$ equivalent to a level of 30 Mx cm^{-2}. If the peak signal within an area lies within one time step from the far-side continuation of the central meridian, the object is taken to represent one or more active regions to be included. If an object extends over more than 12° in longitude, or more than 0.11 in $\sin\,\theta$, it is cut in half in the relevant direction, between its extremes, repeatedly if required. The integrated signal in the residual objects is then used as the total magnetic flux in the region to be introduced into the assimilation at the center of gravity of the object based on the calibrated magnetic flux scaling. An appropriate calibration from time signal δt to magnetic flux Φ contained in the far-side map, derived iteratively by studying 13 relatively isolated regions, was found to be given by: $\Phi = 7.2 \times 10^{20}(\delta t - 1.03)^2$. Newly positioned magnetic bipoles are subsequently taken to consist of a number of smaller flux concentrations, distributed over two touching circular areas, whose size is determined by a specified, fixed flux density; the tilt angle is set to the average value for the ensemble of active regions (see Schrijver, 2001).

Appendix C. Source-Surface Model

We follow the basic strategy outlined first by Schatten, Wilcox, and Ness (1969), enforcing a constant potential at the radius of the source surface, set to 2.5 $R_\odot$ from the center of the Sun. Working in spherical polar coordinates (r, θ', ϕ) (for co-latitude θ'), we extrapolate the magnetic field measured at the photosphere (located at $r = 1$) into the coronal volume above the photosphere out to a spherical source surface at $r = r_s$. If the magnetic field vector $\boldsymbol{B}$ is assumed potential (current-free) within the coronal volume, then $\nabla \times \boldsymbol{B} = 0$, allowing a magnetic potential Φ to be defined for the divergence-free field, is, in spherical coordinates, given by

$$\Phi(r, \theta', \phi) = \sum_{\ell,m} \left[A_\ell^m r^\ell + B_\ell^m r^{-(\ell+1)}\right] Y_\ell^m(\theta', \phi), \tag{1}$$

where the coefficients A_ℓ^m and B_ℓ^m are determined from the imposed radial boundary conditions. The angular variation of Φ is expressed in spherical harmonic functions

$$Y_\ell^m(\theta', \phi) = C_\ell^m P_\ell^m(\cos\,\theta')\, e^{im\phi}, \tag{2}$$

where $P_\ell^m(\cos\theta')$ are associated Legendre functions, and

$$C_\ell^m = (-1)^m \left[\frac{2\ell+1}{4\pi}\frac{(\ell-m)!}{(\ell+m)!}\right]^{\frac{1}{2}}. \tag{3}$$

The photospheric boundary condition for Φ is

$$\left.\frac{\partial\Phi}{\partial r}\right|_{r=1} = -B_r(1,\theta',\phi), \tag{4}$$

thus matching only the radial field (see Wang and Sheeley, 1992). For spherical harmonic coefficients F_ℓ^m of $B_r(1,\theta',\phi)$, such that

$$B_r(1,\theta',\phi) = \sum_{\ell,m} Y_\ell^m F_\ell^m, \tag{5}$$

Equation (4) implies

$$A_\ell^m \ell - B_\ell^m(\ell+1) = -F_\ell^m, \tag{6}$$

where Equation (1) has been used to calculate the radial derivative of Φ. At the source surface, the magnetic field is assumed purely radial, such that $\Phi = 0$ at $r = r_s$, making

$$A_\ell^m r_s^\ell + B_\ell^m r_s^{-(\ell+1)} = 0. \tag{7}$$

Once the coefficients F_ℓ^m are determined, Equations (6) and (7) are solved to yield A_ℓ^m and B_ℓ^m for each (ℓ, m) pair:

$$A_\ell^m = -r_s^{-(2\ell+1)} B_\ell^m\,; \quad B_\ell^m = \frac{F_\ell^m}{1+\ell+\ell r_s^{-(2\ell+1)}}. \tag{8}$$

The magnetic field $\boldsymbol{B}$ anywhere is then given by

$$B_r = -\sum_{\ell,m} Y_\ell^m [A_\ell^m \ell r^{\ell-1} - B_\ell^m(\ell+1) r^{-(\ell+2)}], \tag{9}$$

$$\begin{aligned} B'_\theta = & -\frac{1}{r\ \sin\theta'} \sum_{\ell,m} Y_\ell^m \{R_\ell^m(\ell-1)[A_{\ell-1}^m r^{\ell-1} + B_{\ell-1}^m r^{-\ell}] - \\ & - R_{\ell+1}^m(\ell+2)[A_{\ell+1}^m r^{\ell+1} + B_{\ell+1}^m r^{-(\ell+2)}]\}, \end{aligned} \tag{10}$$

$$B_\phi = -\frac{1}{r\ \sin\theta'} \sum_{\ell,m} im Y_\ell^m [A_\ell^m r^\ell + B_\ell^m r^{-(\ell+1)}], \tag{11}$$

where the step factor R_ℓ^m is defined

$$R_\ell^m = \left[\frac{\ell^2 - m^2}{4\ell^2 - 1}\right]^{1/2}. \tag{12}$$

Appendix D. Other Data in the Movies

Active-region numbers were added based on NOAA/SEC active-region numbers[13]. The top line of the space-weather information at the bottom of each image lists the time for the magnetogram assimilation, the GOES soft X-ray level, the spot coverage (in micro-hemispheres), the proton and electron fluences for the day, the planetary K index, and the Carrington rotation number. The bottom line lists the interplanetary magnetic field strength, latitude and longitude of field vector, and the solar wind temperature, density, and velocity. Values are set to 999 (or comparable) if measurements are not available. Solar, particle, and geomagnetic indices were compiled by NOAA/SEC[14].

Coronal hole boundaries based on the KPNO/KPVT He I 10830 Å observations are shown in light gray for those parts of the map that correspond to the front of the Sun. These maps, based on monthly synoptic charts, were prepared by Karen Harvey and Frank Recely, and made available on the NOAO web sites[15].

The *Yohkoh*/SXT full-disk images were obtained using the Al/Mg (or dagwood) filter.

References

Altschuler, M., Trotter, D., and Orrall, F.: 1972, *Solar Phys.* **26**, 354.
Axford, W. I. and McKenzie, J. F.: 1991, *Solar Wind Seven, Proceedings of the 3rd COSPAR Colloquium*, p. 1.
Balogh, A. and Smith, E. J.: 2001, *Space Sci. Rev.* **97**, 147.
Berger, T. E. and Lites, B. W.: 2002, *Solar Phys.*, in preparation.
Brajša, R., Wöhl, H., Vršnak, B., Ruždjak, D., Sudar, D., Roša, D., and Hržina, D.: 2002, *Solar Phys.* **206**, 241.
Braun, D. C. and Lindsey, C.: 2001, *Astrophys. J.* **560**, L189.
Brouwer, M. P. and Zwaan, C.: 1990, *Solar Phys.* **129**, 221.
DeVore, C. R., Sheeley, N. R., and Boris, J. P.: 1984, *Solar Phys.* **92**, 1.
DeVore, C. R., Sheeley, N. R., Boris, J. P., Young, T. R., and Harvey, K. L.: 1985, *Aust. J. Phys.* **38**, 999.
Golub, L. and Pasachoff, J.: 1997, *The Solar Corona*, Cambridge University Press, Cambridge.
Gosling, J. T.: 1996, *Ann. Rev. Astron. Astrophys.* **34**, 35.
Hagenaar, H. J., Schrijver, C. J., Title, A. M., and Shine, R. A.: 1999, *Astrophys. J.* **511**, 932.
Handy, B. N., Acton, L. W., Kankelborg, C. C. *et al.*: 1999, *Solar Phys.* **187**, 229.
Harvey, K. L.: 1993, Ph.D. Thesis, Astronomical Institute, Utrecht University.
Harvey, K. L. and Zwaan, C.: 1993, *Solar Phys.* **148**, 85.
Hoeksema, J. T.: 1984, Ph.D. Thesis, Stanford University, Stanford, Ca.
Huber, M., Foukal, P., Noyes, R., Reeves, E., Schmahl, E., Timothy, J., Vernazza, J., and Withbroe, G.: 1974, *Astrophys J.* **194**, L115.
Hundhausen, A. J.: 1972, *Coronal Expansion and Solar Wind*, Springer-Verlag, Berlin.

[13]URL: http://www.sec.noaa.gov/majordomo_archive.cgi
[14]URL: http://sec.noaa.gov/ftpdir/indices/old_indices/
[15]URL ftp://ftp.noao.edu/kpvt/synoptic/choles/

Kahler, S. W. and Hudson, H. S.: 2001, *J. Geophys. Res.* **106**, 29239.
Komm, R. W., Howard, R. F., and Harvey, J. W.: 1993, *Solar Phys.* **147**, 207.
Leighton, R. B.: 1964, *Astrophys. J.* **140**, 1547.
Levine, R. H.: 1982, *Solar Phys.* **79**, 203.
Levine, R. H., Altschuler, M. D., Harvey, J. W., and Jackson, B. V.: 1977, *Astrophys. J.* **215**, 636.
Lindsey, C. and Braun, D. C.: 2000, *Solar Phys.* **192**, 261.
Lockwood, M.: 2002, *Astron. Astrophys.* **382**, 678.
Luhmann, J. G., Li, Y., Arge, N., Gazis, P. R., and Ulrich, R.: 2002, *J. Geophys. Res.* **107**, 10.1029.
Mosher, J. M.: 1977, *The Magnetic History of Solar Active Regions*, CalTech, Pasadena, Ca.
Ness, N. F. and Wilcox, J. M.: 1964, *Phys. Rev. Lett.* **13**, 461.
Neugebauer, M., Forsyth, R. J., Galvin, A. B. *et al.*: 1998, *J. Geophys. Res.* **103**, 14587.
Neugebauer, M., Liewer, P. C., Smith, E. J., Skoug, R. M., and Zurbuchen, T. H.: 2002, *J. Geophys. Res.*, in press.
Parker, E. N.: 1958, *Astrophys. J.* **128**, 669.
Schatten, K. H., Wilcox, J. M., and Ness, N. F.: 1969, *Solar Phys.* **6**, 442.
Schrijver, C. J.: 2001, *Astrophys. J.* **547**, 475.
Schrijver, C. J. and Title, A. M.: 2001, *Astrophys. J.* **551**, 1099.
Schrijver, C. J., DeRosa, M. L., and Title, A. M.: 2002, *Astrophys. J.* **577**, 1006.
Schrijver, C. J., Shine, R. A., Hagenaar, H. J., Hurlburt, N. E., Title, A. M., Strous, L. H., Jefferies, S. M., Jones, A. R., Harvey, J. W., and Duvall, T.L: 1996, *Astrophys. J.* **468**, 921.
Schrijver, C. J., Title, A. M., Berger, T. E., Fletcher, L., Hurlburt, N. E., Nightingale, R., Shine, R. A., Tarbell, T. D., Wolfson, J., Golub, L., Bookbinder, J. A., DeLuca, E. E., McMullen, R. A., Warren, H. P., Kankelborg, C. C., Handy, B. N., and De Pontieu, B.: 1999, *Solar Phys.* **187**, 261.
Schwenn, R., Inhester, B., Plunkett, S. P. *et al.*: 1997, *Solar Phys.* **175**, 667.
Sheeley, N. R., Nash, A. G., and Wang, Y.-M.: 1987, *Astrophys. J.* **319**, 481.
Sheeley, N. R., Wang, Y.-M., and Nash, A. G.: 1992, *Astrophys. J.* **401**, 378.
Sheeley, N. R., Bohlin, J. D., Brueckner, G. E., Purcell, J. D., Scherrer, V. S., and Tousey, R.: 1975, *Solar Phys.* **40**, 103.
Švestka, Z., Solodyna, C. V., Howard, R., and Levine, R. H.: 1977, *Solar Phys.* **55**, 359.
Von Steiger, R., Geiss, J., and Gloeckler, G.: 1997, in J. R. Jokipii, C. P. Sonnett, and M. S. Giampapa (eds.), *Cosmic Winds and the Heliosphere*, University of Arizona Press, Tucson, Arizona, p. 581.
Von Steiger, R., Schwadron, N., Fisk, L., Geiss, J., Gloeckler, G., Hefti, S., Wilken, B., Wimmer-Schweingruber, R., and Zurbuchen, T.: 2000, *J. Geophys. Res.* **105**, 27217.
Waldmeier, H.: 1957, *Die Sonnenkorona III*, Birkhäuser Verlag, Basel.
Wang, H., Yan, Y., Sakurai, T., and Zhang, M.: 2000, *Solar Phys.* **197**, 263.
Wang, Y.-M. and Sheeley, N. R.: 1990a, *Astrophys. J.* **355**, 726.
Wang, Y.-M. and Sheeley, N. R.: 1990b, *Astrophys. J.* **365**, 372.
Wang, Y.-M. and Sheeley, N. R.: 1991, *Astrophys. J.* **375**, 761.
Wang, Y.-M. and Sheeley, N. R.: 1992, *Astrophys. J.* **392**, 310.
Wang, Y.-M. and Sheeley, N. R.: 1993, *Astrophys. J.* **414**, 916.
Wang, Y.-M. and Sheeley, N. R.: 1994, *Astrophys. J.* **430**, 399.
Wang, Y.-M. and Sheeley, N. R.: 1995, *Astrophys. J. Lett.* **447**, 143.
Wang, Y.-M. and Sheeley, N. R.: 2002, *J. Geophys. Res.*, in press.
Wang, Y.-M., Lean, J., and Sheeley, N. R.: 2000, *Geophys. Res. Lett.* **27**, 505.
Wang, Y.-M., Nash, A. G., and Sheeley, N. R.: 1989, *Astrophys. J.* 3**47**, 529.
Wang, Y.-M., Sheeley, N. R., and Lean, J.: 2000, *Geophys. Res. Lett.* **27**, 621.
Wilson, P. R., Altrock, R. C., Harvey, K. L., Martin, S. F., and Snodgrass, H. B.: 1988, *Nature* **333**, 748.